Journal of Hematology & Oncology

RESEARCH

Open Access

myCAF-derived exosomal PWAR6 accelerates CRC liver metastasis via altering glutamine availability and NK cell function in the tumor microenvironment

Hongsheng Fang[1,2†], Weixing Dai[1,2†], Ruiqi Gu[1,2†], Yanbo Zhang[1,2†], Jin Li[1,2], Wenqin Luo[1,2], Shanyou Tong[2,3], Lingyu Han[1,2], Yichao Wang[1,2], Chengyao Jiang[1,2], Xue Wang[4*], Renjie Wang[1,2*] and Guoxiang Cai[1,2*]

Abstract

Background Liver metastasis from colorectal cancer (CRC) is a major clinical challenge that severely affects patient survival. myofibroblastic cancer-associated fibroblasts (myCAFs) are a major component of the CRC tumor microenvironment, where they contribute to tumor progression and metastasis through exosomes.

Methods Single-cell analysis highlighted a notable increase in myCAFs in colorectal cancer liver metastases (CRLM). Exosomal sequencing identified PWAR6 as the most significantly elevated lncRNA in these metastatic tissues. In vivo and in vitro assays confirmed PWAR6's roles in CRC cell stemness, migration, and glutamine uptake. RNA pulldown, RIP, and Co-IP assays investigated the molecular mechanisms of the PWAR6/NRF2/SLC38A2 signaling axis in CRC progression, flow cytometry was used to assess NK cell activity and cytotoxicity.

Results Clinically, higher PWAR6 expression levels are strongly associated with increased ^{68}Ga FAPI-PET/CT SUVmax values, particularly in CRLM patients, where expression significantly exceeds that of non-LM cases and normal colon tissues. Regression analysis and survival data further support PWAR6 as a negative prognostic marker, with elevated levels correlating with worse patient outcomes. Mechanistically, PWAR6 promotes immune evasion by inhibiting NRF2 degradation through competitive binding with Keap1, thereby upregulating SLC38A2 expression, which enhances glutamine uptake in CRC cells and depletes glutamine availability for NK cells.

Conclusion myCAFs derived exosomes PWAR6 represents a pivotal marker for CRC liver metastasis, and its targeted inhibition with ASO-PWAR6, in combination with FAPI treatment, effectively curtails metastasis in preclinical models, offering promising therapeutic potential for clinical management.

†Hongsheng Fang, Weixing Dai, Ruiqi Gu and Yanbo Zhang have contributed equally to this work.

*Correspondence:
Xue Wang
wangxuefghc@163.com
Renjie Wang
wangbladejay@sina.com
Guoxiang Cai
gxcaifuscc@163.com
Full list of author information is available at the end of the article

Graphical abstract

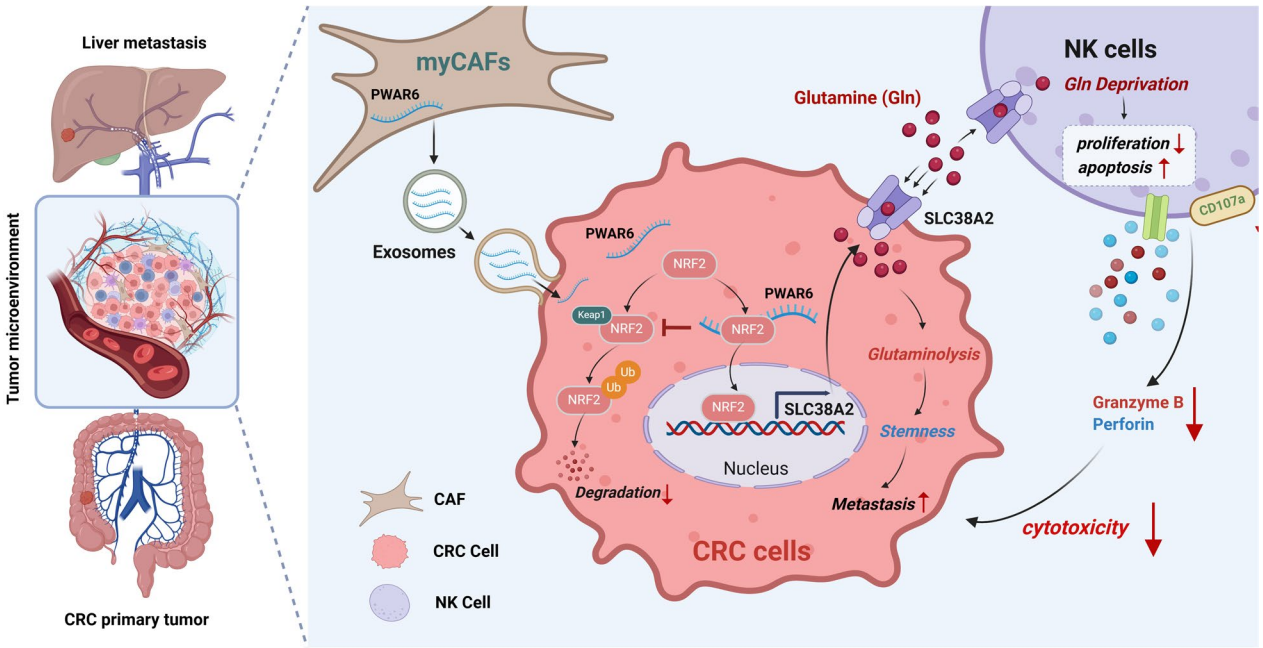

Background

Colorectal cancer (CRC) ranks as the third most prevalent malignancy globally and is the second leading cause of cancer-related mortality [1]. With advances in comprehensive treatment of CRC, the 5-year overall survival (OS) rate for patients with localized CRC now exceeds 90%. In stark contrast, the 5-year OS rate for CRC patients with distant metastases remains dismally low, at less than 15%. Meanwhile, approximately 22% of CRC patients are confronted with the challenge of synchronous distant metastases at the time of initial diagnosis [2, 3]. Thus, understanding key molecules and regulatory mechanisms in the metastatic progression of CRC is essential. These dedicated efforts may hold tremendous promise in early interventions, effective treatments, and improved clinical outcomes of CRC patients.

The intrinsic stemness and metabolic reprogramming are two pivotal characteristics of tumor cells. Cancer stemness is a fundamental characteristic driving the initiation and progression of CRC, featuring its self-renewal capacity and tumor-initiating potential [4, 5]. In our previous work, we also found significant stemness features in metastatic CRC organoids. Inhibiting the pivotal transcription factor SOX2, known for maintaining stem cell properties, could greatly hinder organoid growth and metastatic potential [6]. Regarding the critical role of stemness features in CRC, research targeting cancer stemness may reveal potential therapeutic targets to combat CRC metastasis.

Similarly, metabolic reprogramming is also crucial in driving tumor progression and metastasis. Among these alterations, aberrant glucose and glutamine consumption are the most prevalent metabolic changes observed in CRC [7]. Contrary to the quick utilization of glucose, glutamine is essential for supporting the tricarboxylic acid (TCA) cycle and acts as a vital precursor for lipid, nucleotide, and hexosamine synthesis [8]. Our preliminary research also proved a significant increase in glutamate and its downstream products in CRC tissues, suggesting aberrant activation of glutamine catabolism in CRC cells [9]. Moreover, various studies have also revealed that environmental glutamine deprivation significantly enhances the stemness properties of multiple cancer cells, thereby promoting disease progression [10, 11]. These findings indicate that metabolic alterations in cancer cells not only affect intercellular nutrient metabolism but also profoundly impact intrinsic stemness characteristics.

It is widely acknowledged that CRC cells also establish intricate connections with the peritumoral environment, known as the tumor microenvironment (TME). This milieu comprises cancer-associated fibroblasts (CAF), immune cells, and other nutrient components. Among

these, CAFs have been identified as the most abundant stromal components in the TME which can be classified into different subtypes based on their functions and molecular markers, such as myofibroblastic CAFs (myCAFs), inflammatory CAFs (iCAFs), and antigen-presenting CAFs (apCAFs). MyCAFs are characterized by high expression of α-SMA, FAP, and Collagen I, and are involved in extracellular matrix remodeling, promoting tumor invasion, and contributing to tumor fibrosis. These characteristics make CAFs, particularly myCAFs, important players in cancer progression. The communication between CAFs and CRC cells is often facilitated by extracellular signals, particularly exosomes [12]. Exosomes are small extracellular vehicles (sEVs) with a diameter of 30–200 nm, released by various cells in the TME through the fusion of intracellular vesicles with the plasma membrane. These exosomes can transport essential molecules, including proteins, lipids, and RNAs, significantly influencing the properties of tumor cells [13]. For instance, Hu's work discovered that CRC cells could uptake exosomes containing miR-92a-3p, secreted by CAFs, inducing epithelial-mesenchymal transition (EMT) and facilitating the metastasis of CRC [14]. Additionally, Deng's research also reported that CAFs could enhance chemotherapy resistance in CRC by delivering long noncoding RNA (lncRNA) via exosomes [15]. In our previous study, we discovered that activated CAFs could secrete elevated amounts of pro-inflammatory cytokines, facilitating the metastasis of CRC [16].

Additionally, myCAFs have been reported to reprogram nutrient metabolism not only in tumor cells but also within the TME, influencing the metabolic landscape. To accommodate the augmented glutamine demand of tumor cells, myCAFs actively upregulate anabolic pathways and secrete glutamine into TME, thereby sustaining its supply [17]. Furthermore, myCAFs can inhibit the oxidative phosphorylation process in tumor cells through exosome-mediated mechanisms, which subsequently promotes glutamine-dependent reductive carboxylation [18, 19]. Despite these advances, the specific mechanisms through which myCAFs regulate glutamine metabolism in TME and their effects on tumor stemness in CRC remain poorly understood, underscoring a significant gap in current research.

In the TME, immune cells such as macrophages, natural killer (NK) cells and T cells play multifaceted roles in tumorigenesis, regulated by their activation status and diverse phenotypes. As a fundamental component of anti-tumor immunity, NK cells can directly recognize cells lacking MHC-I molecules and kill tumor cells by secreting granzyme and perforin. Simultaneously, NK cells eliminate infected or tumor cells by releasing perforin to create pores in the target cell membrane, allowing Granzyme B to enter and induce apoptosis [20]. Similar to tumor cells, NK cells and other immune cells also require multiple nutrients in the TME to maintain their function and support anti-tumor activity [21]. However, excessive nutrient uptake by tumor cells can deplete the availability of essential resources for immune cells, thereby profoundly affecting their functions [22]. As a key metabolite, the deprivation of glutamine in the TME impairs the proliferation and growth of activated T cells, while also inhibiting the polarization of M2 macrophages [23, 24]. Nevertheless, the effects of glutamine depletion within the TME on NK cell functionality remain to be elucidated.

To elucidate the complex interactions within the TME, we successfully extracted myCAFs from the liver metastases of CRC patients and normal fibroblasts (NFs) from adjacent healthy liver tissues. We also performed comprehensive screening of lncRNAs encapsulated within exosomes derived from both myCAFs and NFs and metabolomes sequencing of the TME. We identified PWAR6 as a CAF-specific lncRNA, which could regulate the glutamine availability in the TME. Furthermore, we demonstrated the mechanisms underlying the competition of glutamine uptake by CRC cells and NK cells.

Methods

Primary myCAF isolation from CRC

Fresh colorectal cancer tissues were collected after surgical resection, and washed five times in phosphate-buffered saline (PBS) with 20% antibiotic–antimycotic (Gibco, USA), then minced into small pieces using ophthalmic scissors. Subsequently, the tissues were digested with type IV collagenase (Yeasen, China) for approximately one hour at 37 °C at 200 rpm, the digested samples were sequentially filtered through 70 μm cell strainers, the cells were then collected and centrifuged at 1500 rpm for 5 min, and the supernatant was discarded, this step was repeated 2–3 times. (FACS) using antibodies including anti–CD45- APCCy7 (BD Biosciences, no. BD- 557833), anti–EpCAM-P erCP/Cy5.5 (BioLegend, catalog no. 324214), anti–CD31- PECy7 (BioLegend, catalog no. 303118), anti–FAP- APC (primary antibody, R&D Systems, no. MAB3715), or α-SMA (BioLegend catalog no. 614851).

Primary CAFs, which tested negative for EpCAM, CD31, and CD45, and positive for FAP and α-SMA were categorized as myCAFs. These myCAFs was then fully resuspended in DMEM/F12 medium (Gibco, USA) supplemented with 10% fetal bovine serum (FBS) (Gibco, USA) and 1% antibiotics. The tissue suspension was plated into culture dishes, and after 24–48 h, fibroblasts were obtained using a differential time adherent method, as previously reported. After fibroblasts were adequately

prepared, the culture medium was changed daily with DMEM/F12 + FGF (PeproTech, USA). Primary myCAFs were positive for α-SMA, FAP and Collagen I. All samples were obtained from the donors with informed consent, and all related procedures were conducted with the approval of the Ethics Committee of Fudan University Shanghai Cancer Center.

Clinical tissue samples

All samples in FUSCC cohort1, cohort2 and cohort3 were all collected at Fudan University Shanghai Cancer Center and stored at − 80 °C. These samples were approved by the Ethics Committee of Fudan University Shanghai Cancer Center (approval number: 050432-4-1911D).

Exosome extraction and identification

CAFs and NFs were cultured in complete medium (CM) with 10% exosome-free FBS(Gibco, USA). After 72 h, at ~ 90% density, the supernatant was collected and centrifuged at 3000 rpm for 10 min at 4 °C, followed by 10,000×*g* for 30 min at 4 °C to remove the cellular debris. The supernatant was filtered through a 0.22 μm filter (Merck, USA) and ultracentrifuged at 120,000×*g* for 90 min (Thermo Fisher Scientific, USA). Exosome extraction was confirmed by electron microscopy (TEM) and nanoparticle tracking analysis (NTA), and characterized using markers TSG101, HSP70, and Annexin. Exosome-packaged RNA and protein extraction was performed using a Total Exosome RNA and Protein Isolation Kit (Invitrogen, USA).

Plasmids, siRNA, and stable cell line construction

HA-ubiquitin Myc-NRF2 and Flag-Keap1 plasmid was purchased from HANBIO (Wuhan, China). Lentiviral vectors for PWAR6 overexpression (LvPWAR6) and knockdown (shPWAR6) were purchased from Genechem (Shanghai, China). NRF2 shRNA and SLC38A2 shRNA was purchased from Ribobio (Guangzhou, China).

Lentiviral vectors for Keap1 overexpression (LvKeap1) and knockdown (shKeap1) were purchased from Genechem (Shanghai, China). Plasmids and siRNAs were transiently transfected into CRC cells using Lipofectamine 3000 (Invitrogen, USA). All transfection methods were performed according to the manufacturer's protocols.

Multiplex immunofluorescence

The samples were fixed in 4% paraformaldehyde for 15 min, permeabilized with 0.1% Triton X-100 for 10 min (Solar, Beijing), and blocked with 5% BSA (Sigma-Aldrich) in PBS for 1 h to minimize nonspecific binding. Sequential incubation with primary antibodies proceeded overnight at 4 °C starting with anti-panCK (Proteintech), followed by HRP-conjugated secondary antibody (CST) incubation for 1 h at room temperature, and subsequent Tyramide Signal Amplification (TSA) for signal amplification, visualizing in green. HRP activity was quenched with 3% H2O2. This process was repeated for anti-CD3 (Invitrogen, red), anti-α-SMA (CST, yellow), and anti-CD56 (Santa Cruz, pink), each undergoing overnight incubation and TSA signal amplification. Finally, nuclei were counterstained with DAPI (blue). Samples were mounted with an antifade mounting medium for visualization under a fluorescence microscope.

Migration assays

The Transwell assay was performed using a 24-well Transwell plate with 8 μm pore size inserts (Corning, USA). DLD1 and HCT116 tumor cells were cultured in their respective growth media until they reached 70–80% confluence. After detachment using trypsin–EDTA (Gibco, USA), the cells were counted and resuspended in serum-free medium (Gibco, USA) at a concentration of 105 cells/ml. CAFs were cultured similarly, detached, and resuspended in complete medium (with serum) at 104 cells/ml. 600 μl of the complete medium was added to each lower chamber, and 600 μl of the CAF suspension was seeded into the lower chambers, allowing for 1 h of adhesion. The Transwell inserts were then placed into the wells containing CAF cells, and 100 μl of the tumor cell suspension was seeded into each upper chamber. The plate was incubated at 37 °C in a humidified atmosphere with 5% CO2 for 24–48 h. After incubation, non-migratory cells on the upper surface of the membrane were removed using a cotton swab. The migrated cells on the lower surface were fixed with 4% paraformaldehyde for 15 min and stained with crystal violet for 10–15 min. The migrated cells were then visualized and counted under a light microscope (Olympus).

Organoid models and 3D invasion assay

Fresh human CRC tissues were collected and processed by removing excess fat and necrotic tissue. The cleaned tissue was cut into 1–2 mm^3 pieces and digested using a mixture of Collagenase IV (1.5 mg/mL, Sigma-Aldrich, USA)and Dispase (0.1 mg/mL, Sigma-Aldrich, USA) at 37 °C for 30–60 min. The resulting cell suspension was filtered through a 70 μm strainer, centrifuged at 300 g for 5 min, and washed twice with Advanced DMEM/F-12 supplemented with 1% GlutaMAX(Gibco, USA), 10 mM HEPES(Gibco, USA), N2 supplement (Gibco, USA), B27 supplement(Gibco, USA), and 1 mM N-Acetylcysteine (Gibco). The cell pellet was resuspended in Matrigel (Corning, USA)at a concentration of 1×10^4 cells/μL, and 50 μL droplets were plated in a 24-well plate, followed by incubation at 37 °C for 30 min to solidify the Matrigel. Advanced DMEM/F-12 with 50 ng/mL EGF (PeproTech,

USA), 100 ng/mL Noggin (PeproTech, USA), and 500 ng/mL R-spondin 1(PeproTech, USA) was added and refreshed every 2–3 days. Organoids were then embedded in a neutralized 3D fibrillar rat tail collagen I matrix (3 mg/ml, Corning, USA) at a density of 1 organoid per μl and plated in a 24 well glass bottom plate. Collagen gels were allowed to polymerize for 1 h at 37 °C after which organoid media was added to each well.

3D co-culture of tumor organoids and CAFs

First, seed CAFs at an appropriate density onto the bottom of a 24-well plate pre-coated with a thin layer of Matrigel (Corning, USA). The CAFs should be cultured overnight in a medium containing DMEM/F12 (Gibco, USA), 10% FBS (Gibco, USA), and 1% penicillin/streptomycin (Gibco, USA) to allow them to adhere and form a monolayer.

On the following day, carefully remove the CAF medium and add a layer of co-culture matrix on top of the CAF monolayer. This matrix should be a mix of Matrigel and Collagen I (Corning, USA) at a 2:1 ratio, with a final concentration of 3 mg/ml. Next, seed the PDOs, which have been dissociated into single cells or small aggregates (2000–3000 organoid-forming units), as droplets on top of the co-culture matrix.

After establishing the co-culture, slowly add co-culture medium, composed of Advanced DMEM/F12(Gibco, USA), 200 mM GlutaMAX (Gibco, USA), 1 M HEPES (Gibco, USA), 1 × B27(Gibco, USA), 100 ng/ml FGF (PeproTech, USA), 50 ng/ml EGF (PeproTech, USA), and 5% RSPO1 (PeproTech, USA) into each well, ensuring the PDO layer remains stable above the CAF layer.

The co-culture system should be maintained at 37 °C with 5% CO2, during which the medium is regularly changed, and PDO growth is monitored. At the end of the co-culture period, the size and morphology of the organoids can be measured using microscopy or appropriate software to evaluate the impact of CAFs on PDO growth.

Sphere forming assay

Cells were inoculated on 24-well low-adherent plates (Corning, USA) at 1000 cells/well with DMEM/F12(Gibco, USA) medium containing mixed with 4 μg/ml heparin (Sigma Aldrich, USA), 0.48 μ g/ml cortisol (Sigma-Aldrich, USA), 5 ng/ml EGF (Sigma-Aldrich, USA), 5 ng/ml FGF (Sigma-Aldrich, USA) and 10 ng/ml B12 (Sigma-Aldrich, USA). After 10 days of culture, spheres were observed, counted and collected under microscope. For experiments of CRC spheres, spheres were re-digested and seeded into culture plates and subsequently subjected to different treatment.

qRT-PCR assay

Total RNA was extracted from cells using TRIzol reagent (Invitrogen, USA) and treated with DNase I to remove genomic DNA. RNA concentration and purity were assessed with a NanoDrop spectrophotometer. cDNA was synthesized from 1 μg of RNA using the HiScript II Q RT SuperMix for qPCR (Novozan, Nanjing). qPCR was performed in 20 μL reactions containing 2 × SYBR qPCR Master Mix (Novozan, Nanjing), 0.4 μM forward and reverse primers, and 100 ng cDNA. Primers were designed to target specific genes, including GAPDH as an internal control. Reactions were run on an ABI 7500 Fast Real-Time PCR System with the following conditions: 95 °C for 2 min, followed by 40 cycles of 95 °C for 15 s and 60 °C for 1 min. Melt curve analysis confirmed specific amplification. Relative gene expression was calculated using the 2^(−ΔΔCt) method, with data analyzed using GraphPad Prism and statistical significance determined at $P < 0.05$.

The primer sequences are listed in Table S6.

Western blotting

Protein extracted from the cells was electrophoresed by SDS–polyacrylamide gels and was transferred to polyvinylidene difuoride (PVDF) membranes, Next, the membranes were blocked for 2 h at RT with blocking buffer. Membranes were incubated with corresponding primary antibodies overnight at 4 °C, followed by secondary antibodies (1:10,000, Proteintech). Protein–antibody complexes were visualized using an ECL Kit (Yeasen, China). Primary antibodies listed in Table S6.

Pull-down assays

Harvest cells and lyse them in lysis buffer (50 mM Tris–HCl pH 7.5, 150 mM NaCl, 1% NP-40, 0.5% sodium deoxycholate, 0.1% SDS, protease inhibitors) for 30 min on ice. Centrifuge the lysate and collect the supernatant. Incubate the biotinylated PWAR6 probe (Ribobio, China) with streptavidin magnetic beads (CST,USA) at room temperature for 30 min, then wash the beads to remove unbound probes. Incubate the cell lysate with the bead-probe complex overnight at 4 °C. Wash the beads to remove non-specifically bound proteins. Elute the bound proteins by heating the beads in elution buffer (100 mM Tris–HCl pH 8.0, 1% SDS) at 95 °C for 5 min. Analyze the eluted proteins using SDS-PAGE followed by mass spectrometry.

RNA immunoprecipitation

Perform RNA immunoprecipitation (RIP) by lysing cells in RIP lysis buffer (50 mM Tris–HCl pH 7.4, 150 mM NaCl, 1% NP-40, 0.5% sodium deoxycholate, 1 mM EDTA, protease and RNase inhibitors). Incubate the lysate with NRF2 antibody (Proteintech, USA) -conjugated magnetic beads overnight at 4 °C with gentle rotation. Wash the beads to remove non-specifically bound materials. Extract RNA from the immunoprecipitated complex using TRIzol reagent (Thermo Fisher Scientific, USA), and synthesize cDNA using the HiScript II Q RT SuperMix for qPCR (Novozan, Nanjing). Amplify PWAR6 levels by qPCR with specific primers and qPCR Master Mix (Novozan, Nanjing).

CUT&Tag assay

CUT&Tag assay was performed using HyperactiveTM In-Situ ChIP Library Prep Kit for Illumina (TD901-TD902, Vazyme Biotech, China) according to manufacturer's instruction. Briefly, prepared concanavalin A-coated magnetic beads (ConA beads) were added to resuspended cells and incubated at room temperature to bound cells. Non-ionic detergent Digitonin was used to permeate cell membrane. Then, primary NRF2 antibody (Proteintech, 16396-1-AP), Histone antibody (Proteintech, 17168-1-AP) and Normal IgG antibody (Proteintech, 30000-0-AP), secondary antibody and the Hyperactive pA-Tn5 Transposase were incubated with the cells that were bounded by ConA beads in order. Therefore, the Hyperactive pA-Tn5 Transposase can exactly cut off the DNA fragments that were bound with target protein. In addition, the cut DNA fragments can be ligated with P5 and P7 adaptors by Tn5 transposase and the libraries were amplified by PCR with the P5 and P7 primers. The purified PCR products were evaluated using the Agilent 2100. Bioanalyzer (Agilent Technologies, Santa Clara, CA, USA). Finally, these libraries were sequenced on the Illumina NovaSeq6000 platform and 150 bp paired-end reads were generated for the following analysis.

CFSE-based proliferation assay

NK-92MI cells were cultured and prepared for the CFSE-based proliferation assay. The cells were adjusted to a concentration of 1*106 cells/mL in pre-warmed PBS. A stock solution of CellTrace™ CFSE (Invitrogen, C34554) was diluted 1:2000 to obtain a final concentration of 2.5 μM in the cell suspension. The cells were incubated with CFSE for 20 min at 37 °C in a water bath, protected from light. Following incubation, the cells were washed twice with PBS to remove excess CFSE. Subsequently, the cells were cultured in complete medium. After 2 days of culture, CFSE-labeled cells were analyzed by flow cytometry to assess proliferation.

Annexin V/7-AAD apoptosis assay

Apoptosis in NK-92MI cells was assessed using the PE Annexin V Apoptosis Detection Kit (Thermo Fisher Scientific, 88–8102-72) following the manufacturer's instructions. In brief, after 24 h of stimulation, NK-92MI cells were harvested and resuspended in Binding Buffer at a density of $1*10^6$ cells/mL. The cells were then stained with PE-Annexin V and 7-AAD, incubating for 15 min at room temperature in the dark. Subsequently, the stained cells were subjected to flow cytometric analysis.

Preparation of cell suspension from mouse samples

For the isolation of cells from mouse samples, the tissues were finely minced and digested in HBSS containing collagenase IV (MCE, HY-E70005D), DNase I (MCE, HY-108882), and hyaluronidase (Sigma, H6254). The digestion was conducted with shaking at 37 °C for 1 h. Following digestion, the cell suspension was filtered through a 70 μm strainer to remove debris. The resulting cell pellets were treated with RBC lysis buffer (Beyotime, C3702) and then resuspended in PBS for further experimentation.

Flow cytometry and functional analysis of immune cells

For flow cytometric analysis of immune cell populations, cells isolated from mouse samples were first blocked with a blocking buffer (Biolegend, 101320) for 15 min followed by viability staining (Biolegend, 423105). Subsequently, surface marker staining was performed to identify specific immune cell subsets. The gating strategy used included the following populations: NK cells (CD45+, NK1.1+, CD3-), CD8+ T cells (CD45+, CD8+, CD3+), CD4+ T cells (CD45+, CD4+, CD3+), macrophages (CD45+, CD11b+, Ly6g-, F4/80hi) and B cells (CD45+, CD19+).

For functional analysis, immune cells were stimulated using the Cell Activation Cocktail (BioLegend, 423303) for 4 h. After stimulation, the cells were blocked using a blocking solution (BioLegend, 101320) to prevent non-specific binding. Subsequently, viability staining was performed using the Zombie NIR™ Fixable Viability Kit (BioLegend, 423105). The cells were then stained for surface markers with the appropriate antibodies. Then the cells were fixed with Fixation Buffer (BioLegend, 420801). Finally, intracellular staining was conducted using the corresponding antibodies for the desired intracellular markers. Flow cytometry was then performed to assess the activation and functionality of the immune cells.

LDH cytotoxicity assay

This assay was performed using an LDH cytotoxicity kit (C0016, Beyotime). HCT116 and DLD1 (target cells, 5*104 cells/ml) were cocultured for 2 h with NK-92MI at E:T ratios of 1:1, 2:1, 5:1, and 10:1 in 96-well plates. After incubation, supernatants from each well were collected and analyzed according to the manufacturer's instructions to assess cytotoxicity.

Animal models

5-weekold female C57BL/6 mice were purchased from Shanghai Experimental Animal Center and maintained under standard conditions according to protocols approved by the Institutional Animal Care and Use Committee of Fudan university Shanghai Cancer Center (approval number: FUSCC-IACUC-S20210022).

The subcutaneous xenograft mice model was established to evaluate tumor formation in vivo. The in vivo metastatic ability was investigated using splenic injection experiments. For the subcutaneous tumor model, 1×10^6 mixture of CAFs and MC38 cells were suspended in 100 μL of PBS and injected into the right flank of each mouse. Tumor growth was monitored regularly, with measurements taken at specific intervals to assess progression. For the liver metastasis model, 1×10^6 mixture of CAFs and MC38 cells in 100 μL of PBS were injected directly into the spleen. Following injection, the spleen was left in situ for 5 min to allow the cells to disseminate to the liver. The spleen was then removed to prevent primary tumor formation at the injection site.

7 days after the inoculation, tumor-bearing mice were administered shRNA intraperitoneally at a dose of 1.5 mg/kg/week using the Invivofectamine 3.0 liposomal delivery system (Thermo Fisher Scientific, IVF3001). The shRNA was mixed thoroughly with the Invivofectamine reagent prior to intraperitoneal administration. Besides, tail vein injections of a scrambled ASO or the inhibitor ASO-PWAR6 (10 nmol per injection, RiboBio) were performed in the mice every 3 days. FAPI (20ug per injection, MCE) was administered orally twice daily. All of the mice were euthanized 6 weeks post-injection, thereafter, the tumors were weighed. All harvested tissues were used for pathological analysis.

Development of myCAF score

Based on the 596 genes that were closely related to myCAF in colorectal cancer patients reported by Herrera's team [25], we used these genes and the Lasso Cox algorithm to construct a myCAF score consisting of 40 genes. The median value of myCAF score was used to divide patients in high-myCAF and low- myCAF groups. After that, we utilized clinicopathological data and conducted gene ontology (GO) analyses as well as Kaplan–Meier (K-M) survival curves to validate our myCAF score in both TCGA and meta-GEO cohorts. In statistical analysis, we performed the Log-Rank test for survival analysis, and the Wilcoxon test was used to demonstrate the differences in gene expression between two groups. Additionally, the chi-squared test was applied when comparing proportion-related data.

Non-coding RNA analysis in GSE39582

Published noncoding RNA-seq data, particularly for PWAR6, is only available in the GSE39582 dataset and not in the TCGA database. Therefore, we exclusively used the GSE39582 dataset to assess the correlation between PWAR6 expression and the myCAFscore, as shown in Fig. 3I. Student's t-test or one-way analysis of variance (ANOVA) was used to evaluate the significance of differences between groups.

Statistical analysis

All described results are representative of at least three independent experiments. Data are presented as means ± Standard Error of the Mean (s.e.m.). Statistical analyses were performed using SPSS 22.0 software (SPSS) or GraphPad Prism 99 software (GraphPad). Student's t-test or one-way analysis of variance (ANOVA) was used to evaluate the significance of differences between groups. A chi-squared test was used to evaluate the correlation between PWAR6 expression and clinicopathological characteristics, univariate and multivariate Cox proportional hazard regression models were used to evaluate the effects of PWAR6 expression or other clinicopathological parameters on survival and the hazard ratio (HR), correlations were detected by Spearman's correlation coefficient, overall survival (OS) was assessed by the Kaplan– Meier method and log-rank test. All P values are $^*P<0.05$, $^{**}P<0.01$, $^{***}P<0.001$.

Results

myCAFs enhanced CRC cell stemness and promote migration

To investigate the role of CAFs in CRC, we utilize single-cell sequencing data obtained from GSE166555 (comprising scRNA-seq profiles of tumor and adjacent normal tissue from 12 CRC patients without liver metastasis) and GSE178318 (encompassing scRNA-seq profiles of primary CRC, matched liver metastases, and blood samples from 6 CRC patients with liver metastases),clustering analysis found that the proportion of CAFs is higher in CRC patients with liver metastasis (CRLM) than those without LM. Specifically, myCAFs are significantly elevated in CRLM, while changes in iCAFs, apCAFs, and other CAFs are not as pronounced. (Fig. 1A, B). In the meta-GEO and TCGA cohort, a myCAF score was

established to evaluate the levels of myCAFs in the bulk RNA-seq data. Patients with higher myCAF scores are predominantly diagnosed with CRC at stage III and IV, whereas those with lower myCAF scores are primarily in stages I and II. Kaplan–Meier analysis reveals that elevated myCAF scores are associated with significantly poorer prognoses in CRC patients (Fig. 1C, D, Supplementary Figure 1A).

To investigate the influence of myCAFs on CRC progression in detail, we isolated myCAFs and normal fibroblasts (NFs) from CRC tissues and corresponding adjacent normal tissue. Additionally, organoid models were derived from the corresponding CRC tissues, following established methods (Fig. 1E). To confirm the identity of our NFs and myCAFs, we performed western blotting analysis to verify the expression of specific myCAFs biomarkers, including α-SMA, FAP, and Collagen I [26] (Fig. 1F). The data indicated that the myCAFs we extracted exhibited higher levels of these markers compared to NFs. We also assessed the cellular morphology of the two fibroblast types using light microscopy and immunofluorescence (IF) techniques. Under normal microscopy, both myCAFs and NFs displayed a similar spindle-shaped morphology (Fig. 1G, left). However, IF assays revealed that myCAFs showed higher fluorescence intensity for these markers (Fig. 1G, right). Furthermore, we utilized multicolor fluorescence staining of tissue samples from CRC patients with and without LM, to assess the proportion of myCAFs in the TME. The results also confirmed a substantial enrichment of myCAFs in CRLM patients, characterized by the red fluorescence of α-SMA (Fig. 1H).

Subsequently, we employed both cell lines and organoid models to investigate the influence of myCAFs on CRC cells within the tumor microenvironment. In the cell line experiments, we utilized well-established protocols to establish a non-contact co-culture system involving two CRC cell lines and the isolated myCAFs [27] (Fig. 1E). Notably, CRC cells co-cultured with myCAFs demonstrated a significant enhancement in migratory capacity, increased sphere formation, and elevated expression of stemness markers, suggesting that myCAFs enhance CRC cell stemness and promote metastasis in vitro (Fig. 1I-L, Supplementary Figure 1B-K). Additionally, we incorporated myCAFs into the patient-derived organoid (PDO) 3D invasion matrix using previously validated methodologies. The PDOs co-cultured with myCAFs exhibited markedly more pronounced protrusive migration into the matrix compared to those without myCAFs co-culture (Fig. 1M, N). These observations provide compelling evidence that myCAFs substantially augment the metastatic potential of CRC cells in vitro.

Finally, we employed subcutaneous tumor models and LM models in nude mice to validate the effects of CAFs in vivo. After co-injecting myCAFs with CRC cells, the mice were randomly divided into two groups: the Fibroblast Activation Protein Inhibitor (FAPI) group and the saline group. FAP is highly expressed in stroma component of TME, especially in the myCAFs. FAPI has demonstrated potential in both inhibiting fibroblast activation and diagnosing metastases in various cancer types [28]. The mice in the FAPI group were administered FAPI inhibitor orally, while the mice in the saline group were administered saline. Our results showed that the size of subcutaneous tumors and liver metastases in the FAPI group was smaller than those in the physiological saline group (Fig. 1O–R).

These findings strongly emphasize the critical role of myCAFs in the metastasis of CRC, elucidating potential

(See figure on next page.)

Fig. 1 myCAFs enhanced CRC cell stemness and promote migration. **A** Uniform manifold approximation and projection (UMAP)plot showing the eight major cell types. Dots represent individual cells and colors represent different cell populations. (n = 18 patients). **B** Single cell data clustering analysis, data from GSE16655 and GSE178318. (n = 18 patients). **C** Proportion of patients with different Stages in high myCAF and low myCAF score groups, data obtained from the metaGEO database. (n = 913 patients). **D** Kaplan—Meier survival curve of patients with high myCAF score and low myCAF score, data obtained from the metaGEO database. (n = 913 patients). **E** Workflows of the procedure for extracting myCAF and PDOs from CRC Patients and assessing invasion capability after co-culture with CRC Cells. **F** Western blot analysis of α-SMA, FAP and Collagen I protein expressions in NFs and myCAFs isolated from CRC patients. (myCAF and NF were isolated from four patients). **G** Immunofluorescence analysis of α-SMA, FAP and Collagen I protein expressions in NFs and myCAFs isolated from CRC patients. Scale bars = 100μm (left), Scale bars = 20μm (right). (n = 3, one of three biological replicates). **H** Representative α-SMA staining in CRC tissues from FUSCC cohort 2. Scale bars = 50μm. (n = 3, one of three biological replicates). **I**, **J** Transwell assay to evaluate the invasion after co-cultured DLD1 with myCAFs. Scale bars = 100μm. (Representative images are shown, data are from five biologically replicates). **K**, **L** Sphere forming assay to evaluate the stemness after co-cultured DLD1 with myCAFs. Scale bars = 100μm. (Representative images are shown, data are from five biologically replicates). **M**, **N** PDOs 3D invasion assay to evaluate the invasion of PDOs after co-cultured PDOs with myCAFs. Scale bars = 50μm. (Representative images are shown, data are from three replicates). **O**, **P** Representative images of subcutaneous tumors treated with FAPI gavage. (n = 5 mice per group). **Q**, **R** Liver metastasis assays were performed in vivo by splenic injection to evaluate the effect of FAPI on tumor metastasis. (n = 5 mice per group). Data are shown as mean ± s.e.m. For B-C, data were analyzed by chi-square test. For D, data were analyzed by log-rank test. For I-R, data were analyzed by two-tailed Student's t-test. *P* values. **P* < 0.05, ***P* < 0.01, ****P* < 0.001

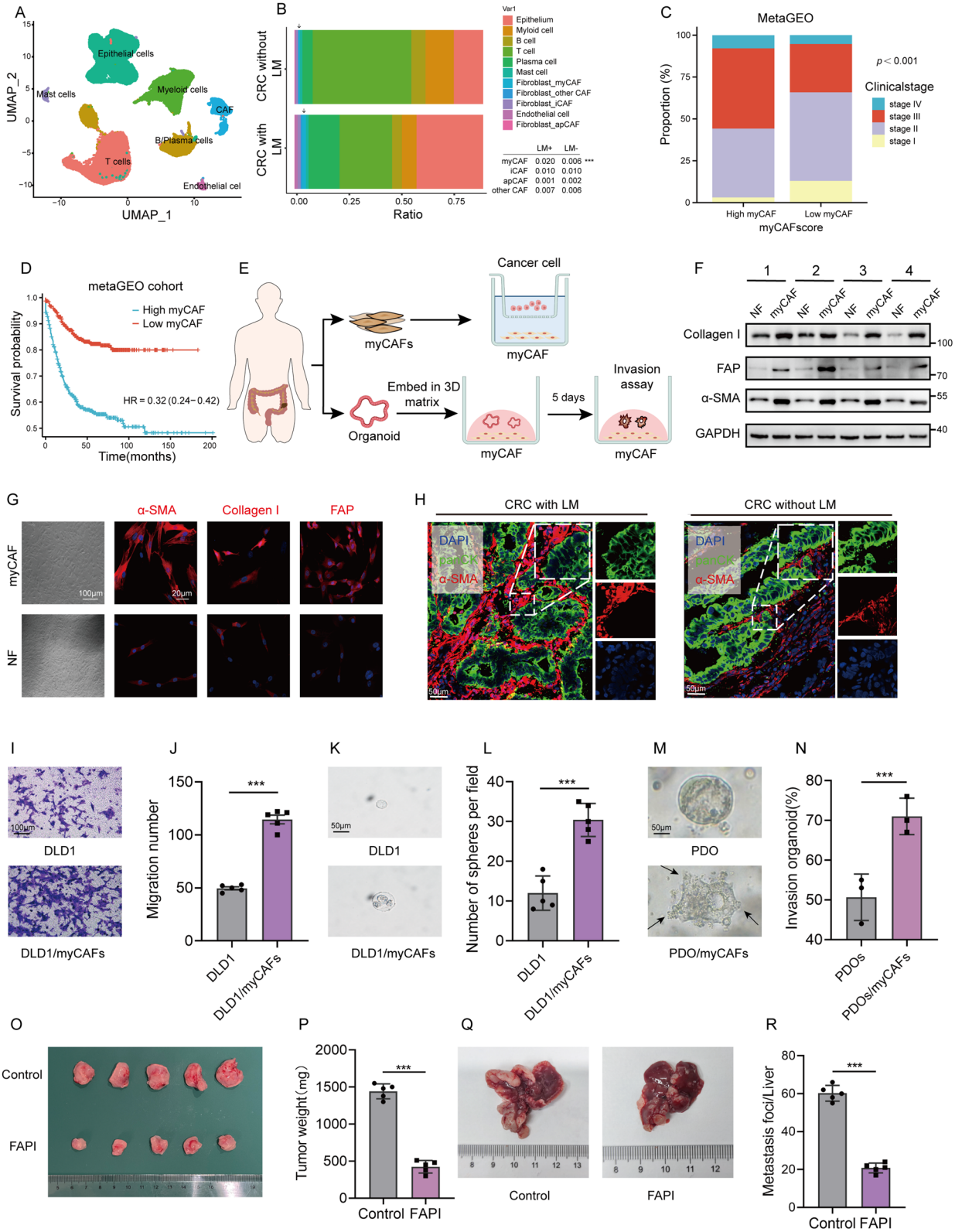

Fig. 1 (See legend on previous page.)

avenues for therapeutic interventions targeting the dynamic interplay of myCAFs and CRC cells on tumor progression.

myCAF-derived exosome PWAR6 enhanced cell stemness and promote CRC cell migration

As previously introduced, exosomes are the primary vehicles for communication between myCAFs and other components of the TME. Using our previously established myCAFscore, we performed differential gene expression and pathway enrichment analyses on samples from the meta-GEO cohort with high and low myCAFscore. Pathways related to exosome biogenesis and secretion are highly upregulated in samples with higher myCAFscore (Supplementary Figure 2A).

To elucidate whether exosomes also contribute to our pervious finding, we co-cultured myCAFs with CRC cells in the presence of the exosome inhibitor GW4869 (Supplementary Figure 2B-C). Strikingly, subsequent Transwell and sphere formation assays showed that adding GW4869 to the co-culture system reversed the migration rate and stemness properties of CRC cells (Fig. 2A–C, Supplementary Figure 2D-H). Next, we isolate exosomes from myCAFs and co-culture them with DLD1/HCT116 cells. Similarly, we found that exosomes can promote the metastasis and stemness of these cells (Supplementary Figure 2I-M). In our 3D invasion experiments with PDOs, the addition of GW4869 to the co-culture system also significantly reversed the protrusive migration (Fig. 2D), suggesting that myCAFs facilitate metastasis and enhance stemness in CRC cells via exosome.

To elucidate the mechanisms of myCAF-derived exosomes (CAF-Exo) on CRC cells, we collected five pairs of CRLM tissues and adjacent normal liver tissues, successfully extracting NFs and myCAFs from these samples. After that, exosomes from the conditioned medium of myCAFs and NFs were isolated through ultracentrifugation [29] (Fig. 2E). To ensure that exosomes were successfully extracted, we performed Western blotting to assess the presence of several key markers in the isolated exosomes, including TSG101, HSP70, and Annexin [30] (Fig. 2F). Transmission electron microscopy (TEM) was also used to directly observe the membrane structure of exosomes secreted by myCAFs and NFs, which appeared as closed, round vesicles (Fig. 2G).

We then performed non-coding RNA sequencing on exosomes derived from myCAFs and normal fibroblasts (NF-Exo). Among all the detected lncRNAs, PWAR6 exhibited the most significant upregulation in myCAF-Exo compared to NF-Exo (Fig. 2H). To confirm these findings, we assessed PWAR6 expression levels across various samples, including myCAFs, NFs, CAF-Exo, NF-Exo, CRC cell lines, a healthy intestinal epithelial cell line, CRC tumor tissues, and adjacent normal tissues. Consistently, PWAR6 expression was significantly higher in CAFs, myCAF-Exo, and CRC tumor tissues, with no notable difference observed between CRC cell lines and the healthy intestinal epithelial cell line (Fig. 2I). In the GSE41568 dataset, PWAR6 expression was also significantly upregulated in CRC metastases compared to primary tumors (Supplementary Figure 3A). These findings underscore the substantial upregulation of PWAR6 in myCAFs and myCAF-Exo, suggesting its potential role in CRC tumor progression. Additionally, the FISH assay on PDO and CRC cells revealed that PWAR6 is primarily localized in the nucleus (Fig. 2J).

To investigate the biological function of exosomal-PWAR6 in CRC, we utilized short hairpin RNA (shRNA)

(See figure on next page.)

Fig. 2 myCAF-derived exosome PWAR6 enhanced glutamine uptake and promote CRC cell migration. **A**–**C** Evaluation of invasion and stemness of DLD1 Cells after GW4869 treatment using Transwell and spheroid formation assays. Scale bars = 100μm(upper), Scale bars = 50μm(lower). (Representative images are shown, data are from five biologically replicates). **D** PDO 3D invasion assay to evaluated the invasion of PDOs after GW4869 treatment. Scale bars = 50μm. (Representative images are shown, data are from three biologically replicates). **E** Workflows of the extraction of fibroblasts from LM tissues (myCAFs) and adjacent normal tissues (NFs) in CRLM patients, followed by the extraction of exosomes for lncRNA sequencing and metabolomics analysis. **F** Expression of the exosome markers TSG101, HSP70 and Alix confirmed by western blot. (n = 3, one of three biological replicates). **G** Transmission electron microscopy (TEM) images of exosomes secreted from myCAFs and NFs. Scale bars = 100nm. (n = 3, one of three biological replicates). **H** Top 100 upregulated and downregulated lncRNAs in exosomes secreted by myCAFs from CRLM tissues and paired NFs. **I** The expression levels of PWAR6 among normal colonic epithelial cell line (NCM460), CRC cell lines, CRC tissues (T), normal intestinal epithelial tissues (N), NFs, NF-derived exosomes, myCAFs, and myCAF-derived exosomes. (n = 3 technical replicates, one of three biological replicates). **J** ISH experiments in CRC cells and PDO indicate that PWAR6 is localized in both the nucleus and the cytoplasm. Scale bars = 100μm. (n = 3, one of three biological replicates). **K** Knockdown of PWAR6 in myCAFs. (n = 5, one of three biological replicates). **L** Knockdown of PWAR6 in myCAFs reduces its level in exosomes secreted by myCAFs. (n = 5, one of three biological replicates). **M** Incubation with exosomes from PWAR6-knockdown myCAFs significantly reduces PWAR6 levels in DLD1 cells. (n = 5, one of three biological replicates). **N**, **O** PDO 3D invasion assay to evaluated the invasion of PDOs after knocking down PWAR6. Scale bars = 50μm. (Representative images are shown, data are from three biologically replicates). **P**, **Q** PWAR6 knockdown significantly reduces the size of subcutaneous tumors. (n = 5 mice per group). **R**, **S** PWAR6 knockdown significantly reduces the size of liver metastases. (n = 3 mice per group). Data are shown as mean ± s.e.m. For A-D, I and K–O, data were analyzed by one-way ANOVA. For P-S, data were analyzed by two-tailed Student's t-test. *P* values. **P* < 0.05, ***P* < 0.01, ****P* < 0.001

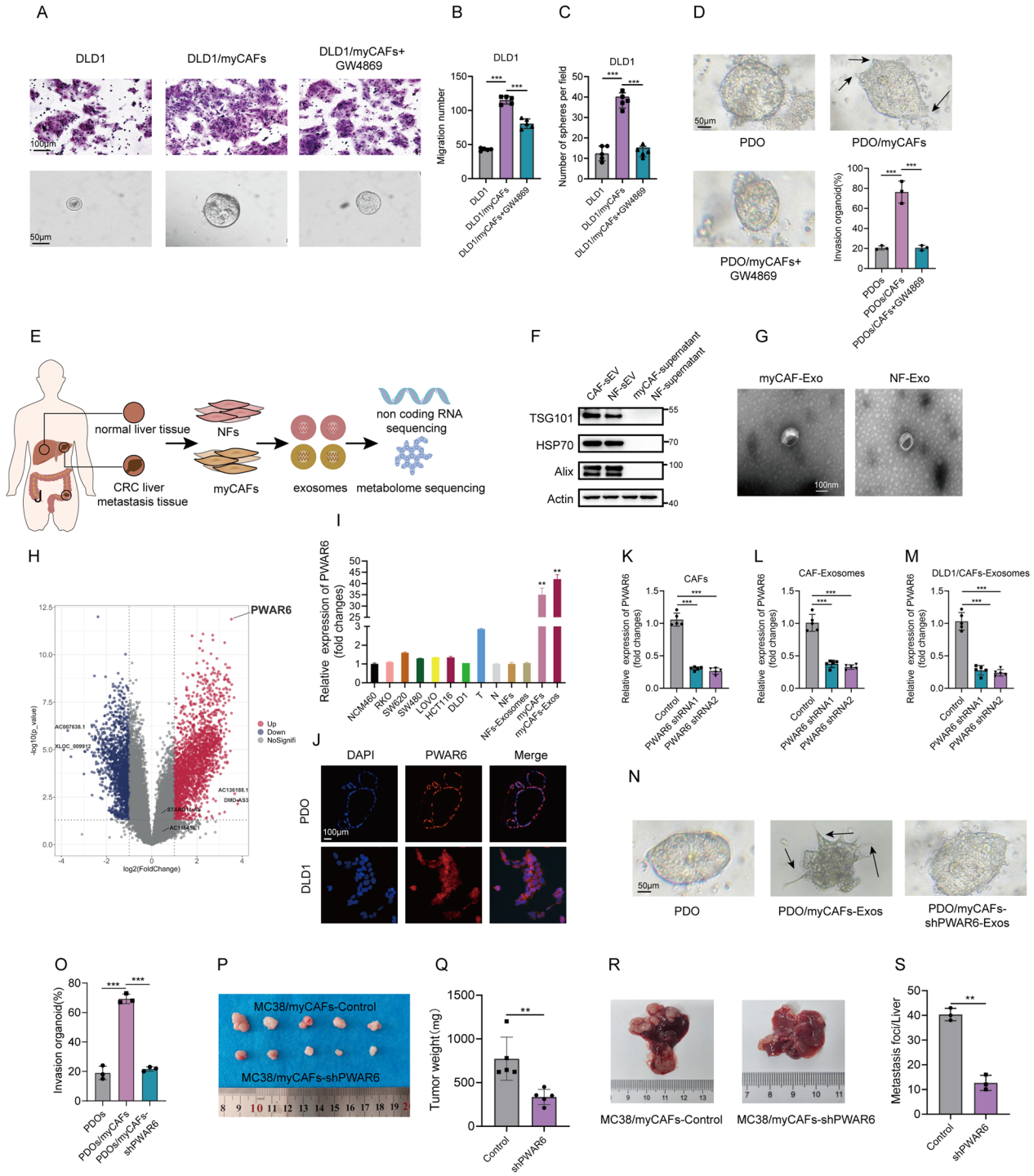

Fig. 2 (See legend on previous page.)

to knock down the expression of PWAR6 in CAFs (Fig. 2K) and observed a corresponding decrease in the levels of PWAR6 in the secreted exosomes from myCAFs (Fig. 2L). Moreover, we co-cultured the myCAFs after PWAR6 knockdown and unmodified myCAFs with both CRC cell lines and PDOs (Fig. 2M and Supplementary Figure 3B-C). After co-culturing with PWAR6-knockdown myCAFs, the protrusive migration of PDOs into 3D matrix was significantly reduced, compared to the control group (Fig. 2N, O). Likewise, CRC cells

co-cultured with PWAR6-knockdown myCAFs exhibited reduced migration and sphere formation abilities (Supplementary Figure 3D-I), along with significantly decreased expression of stemness and epithelial-mesenchymal transition markers (Supplementary Figure 3J-L). These in vitro experiments demonstrated that myCAF-derived exosome PWAR6 could enhance stemness and metastatic potential in colorectal cancer.

Subsequently, MC38 cells were co-cultured with either PWAR6-knockdown or unmodified myCAFs, then injected subcutaneously and into the spleens of C57BL/6 mice. We observed a significant decrease in the number and weight of liver metastases and subcutaneous tumors in the MC38/myCAFs-shPWAR6 group compared to the control group (Fig. 2P–S). Immunohistochemical staining (IHC) was also performed on the liver metastases of mice. The analysis revealed a remarkable decrease in the expression of Vimentin and N-cadherin, while E-cadherin expression was notably increased in the MC38/myCAFs-shPWAR6 group (Supplementary Figure 3M-N).

In summary, our findings reveal that myCAF-derived exosome PWAR6 promotes CRC stemness and metastasis in both in vitro and in vivo experiments.

Expression of exo-PWAR6 and its clinical significance in CRC patients

As previously introduced, FAPI shows potential as a novel radiotracer for tracking myCAFs and tumor lesions [31]. Recently, ^{68}Ga-FAPI Positron Emission Tomography (^{68}Ga-FAPI-PET) has been developed and clinically applied for imaging metastases and diagnosing tumors [32]. In our study, we conducted a comprehensive analysis of PWAR6 levels in histopathological samples from 15 patients with different ^{68}Ga-FAPI-PET SUVmax values from the Fudan University Shanghai Cancer Center (FUSCC Cohort1). We found that the expression levels of PWAR6 were significantly higher in patients with elevated SUVmax values and lower in those with reduced SUVmax values (Fig. 3A, B). Besides, we also compared the organoid derived from these patient tissues. A higher number of organoids were observed from patients with elevated ^{68}Ga-FAPI-PET SUVmax values (Fig. 3C left). Moreover, these organoids exhibited a higher positivity rate of PWAR6 (Fig. 3C right). Besides, we also demonstrated that samples with higher myCAF scores in GSE39582 exhibited correspondingly elevated expression levels of PWAR6 (Fig. 3I).

Next, we collected tissue samples from 5 paired normal tissues, 10 patients with non-LM CRC, and 10 CRLM patients (FUSCC cohort2). After extracting exosomes from the tissues, we used qPCR to measure PWAR6 expression in these samples. Meanwhile, we employed the chromogenic in situ hybridization (CISH) method to compare PWAR6 expression in their intestinal tissues. The results of qPCR and CISH both indicated patients with CRLM has the highest PWAR6 expression, followed by those with non-metastatic CRC and lowest in patients with enteritis (Fig. 3D, E). Representative abdominal magnetic resonance imaging (MRI) or computed tomography (CT) images of these patients are shown in Fig. 3F.

Subsequently, we investigated the pathological implications and prognostic value of PWAR6 in a separate FUSCC cohort comprising 150 paraffin-embedded CRC tissues of stages I-IV that were carefully preserved in a −80 °C refrigerator (FUSCC cohort3). Kaplan–Meier survival analysis based on FUSCC cohort3 demonstrated a clear distinction in the clinical outcomes between patients with low and high expression levels of PWAR6. Patients with low PWAR6 expression exhibited a significantly better overall survival (OS) compared to those with high expression (Fig. 3J). To further investigate the associations between PWAR6 expression and key clinicopathological factors, we conducted a Chi-square test. Our analysis revealed that distant metastasis (M stage), survival, neural invasion, vascular invasion, age and tumor size were significantly associated with PWAR6 expression (Fig. 3G). We next performed univariate and multivariate Cox regression analyses of OS in the FUSCC cohort 3. In univariate Cox regression analysis, M stage and PWAR6 expression levels were significantly associated with prognosis ($P < 0.05$). Multivariate Cox regression analysis

(See figure on next page.)

Fig. 3 Expression of exo-PWAR6 and its clinical significance in patients with CRC. **A**, **B** Representative image and PWAR6 expression of patients with varied ^{68}Ga-FAPI-PET SUV max values (n = 15 patients). **C** Representative image of PDOs and PWAR6 ISH using tissues from patients with varied ^{68}Ga-FAPI-PET SUV max values. Scale bars = 50μm. (n = 15 patients). **D**, **E** Representative ISH image and PWAR6 expression in healthy donors (enteritis) and CRC patients with and without LM. Scale bars = 50μm (n = 25 patients). **F** Representative CT or MRI Images of CRC Patients with and without LM (n = 25 patients). **G** Heatmap of Chi-Square test based on the association between PWAR6 and different clinicopathological factors. (n = 150 patients). **H** Univariate and multivariate Cox regression analyses of OS in the FUSCC cohort 3. (n = 150 patients). **I** PWAR6 expression level of patients with high myCAF score and low myCAF score, data obtained from the GSE39582. (n = 133 patients). **K** Kaplan–Meier survival curve of patients with PWAR6-high and PWAR6-low, data obtained from the FUSCC cohort3. (n = 150 patients). Data are shown as mean ± s.e.m. For A-D and **I**, data were analyzed by one-way ANOVA. For G, data were analyzed by Chi-square test. For H, data were analyzed by Cox regression analysis. For **J**, data were analyzed by log-rank test. *P* values. **P* < 0.05, ***P* < 0.01, ****P* < 0.001

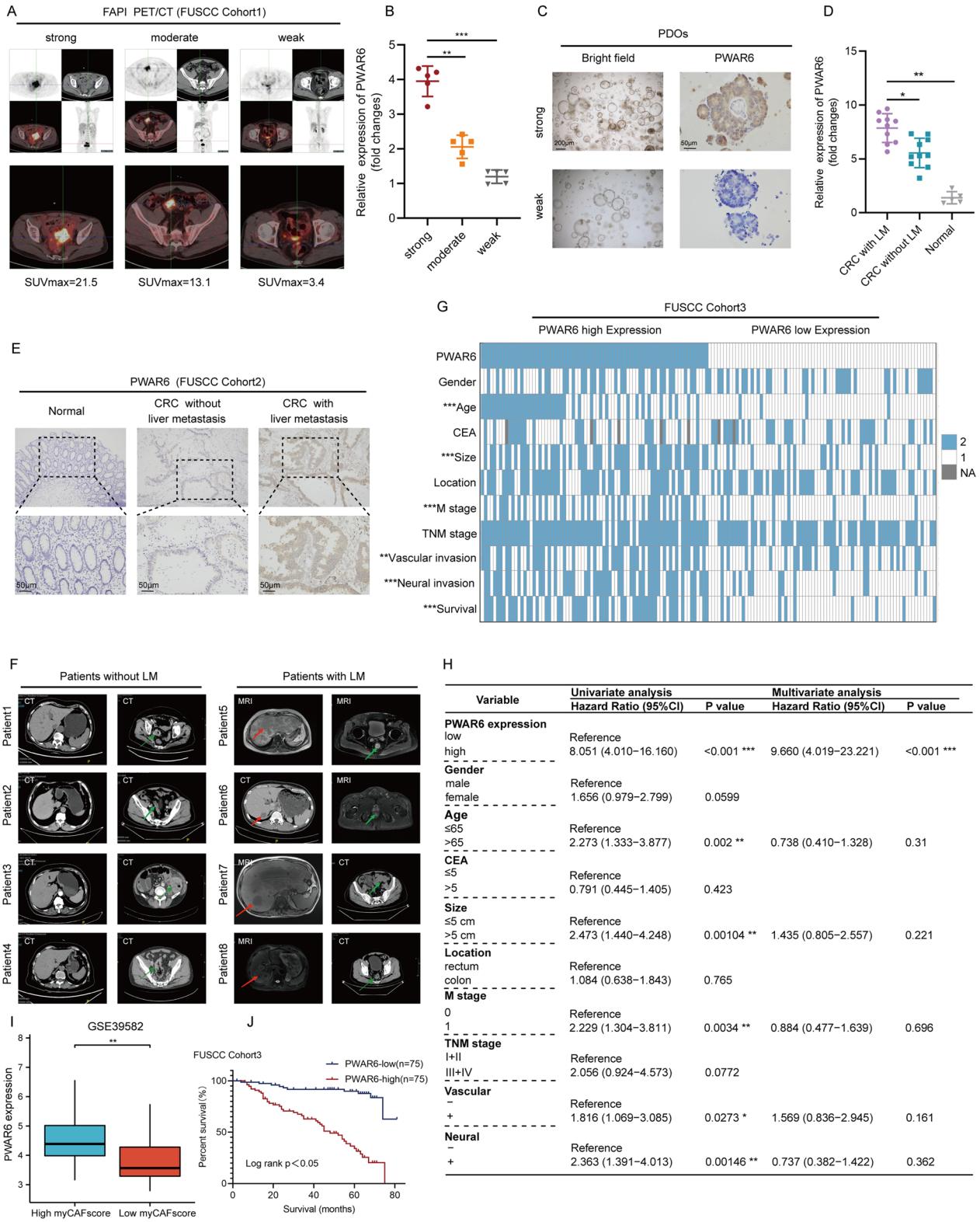

H

Variable	Univariate analysis		Multivariate analysis	
	Hazard Ratio (95%CI)	P value	Hazard Ratio (95%CI)	P value
PWAR6 expression				
low	Reference			
high	8.051 (4.010−16.160)	<0.001 ***	9.660 (4.019−23.221)	<0.001 ***
Gender				
male	Reference			
female	1.656 (0.979−2.799)	0.0599		
Age				
≤65	Reference			
>65	2.273 (1.333−3.877)	0.002 **	0.738 (0.410−1.328)	0.31
CEA				
≤5	Reference			
>5	0.791 (0.445−1.405)	0.423		
Size				
≤5 cm	Reference			
>5 cm	2.473 (1.440−4.248)	0.00104 **	1.435 (0.805−2.557)	0.221
Location				
rectum	Reference			
colon	1.084 (0.638−1.843)	0.765		
M stage				
0	Reference			
1	2.229 (1.304−3.811)	0.0034 **	0.884 (0.477−1.639)	0.696
TNM stage				
I+II	Reference			
III+IV	2.056 (0.924−4.573)	0.0772		
Vascular				
−	Reference			
+	1.816 (1.069−3.085)	0.0273 *	1.569 (0.836−2.945)	0.161
Neural				
−	Reference			
+	2.363 (1.391−4.013)	0.00146 **	0.737 (0.382−1.422)	0.362

Fig. 3 (See legend on previous page.)

further identified high PWAR6 expression as an independent predictor of poor OS (Fig. 3H).

Our study highlights that elevated PWAR6 expression, as assessed by 68Ga-FAPI-PET and IHC analysis, correlates with worse DFS and OS in CRC patients. Elevated PWAR6 levels are significantly correlated with a higher proportion of CAFs and adverse clinicopathological features among CRC patients.

CAF-derived exo-PWAR6 enhances the glutamine uptake of CRC cells via upregulation of amino acid transporters SLC38A2

Metabolomic sequencing data on previous myCAF-Exo and myNF-Exo elucidated notable differences in the glutamine metabolism pathways between myCAFs in liver metastases and NFs in normal liver tissues (Fig. 4A, B).

Glutamine metabolism, involving a series of interconnected reactions, holds crucial implications. Notably, exogenous glutamine primarily enters cancer cells through the family of glutamine transporters. Once internalized, glutamine undergoes conversion to glutamate, which is subsequently catabolized to α-ketoglutarate (α-KG) and enters the tricarboxylic acid (TCA) cycle.

Encouragingly, our findings revealed a significant increase in glutamine uptake, as well as elevated levels of glutamate and α-ketoglutarate in CRC cells co-cultured with myCAFs, but the enhancement could be reversed by knocking down PWAR6 in CAFs (Fig. 4C, D).

This suggests an active modulation of glutamine metabolism in the presence of myCAF-derived PWAR6, likely contributing to the altered metabolic phenotype and tumor progression observed in CRC.

Subsequently, we postulated that PWAR6 might influence glutamine influx through the regulation of amino acid transporters. Glutamine transporters belonging to the solute carrier (SLC) family play a crucial role in mediating glutamine transport. To investigate this, we performed qRT-PCR to analyze the transcriptional profiling of known glutamine transporters in DLD1/HCT116 cells. We found that only SLC38A2 exhibited downregulated/upregulated expression at mRNA when DLD1/HCT116 cells were treated with shPWAR6/LvPWAR6 exosomes derived from myCAFs (Fig. 4E).

Western blot revealed that silencing PWAR6 attenuated SLC38A2, whereas overexpressing PWAR6 enhanced their expressions in DLD1/HCT116 cells treated with myCAF exosomes (Fig. 4F, G). In the GSE41568 dataset, SLC38A2 expression was also significantly upregulated in CRC metastases compared to primary tumors (Fig. 4H). Additionally, immunofluorescence assay showed that NRF2 co-localizes with SLC38A2 in the nucleus of DLD1 cells (Fig. 4I). More importantly, increase in glutamine uptake, cell migration and cell stemness by PWAR6 overexpression could be partially reversed by SLC38A2 knockdown (Fig. 4J–L and Supplementary Fig. 4A-G).

Next, we further explore the clinically significant of SLC38A2 using our previous FUSCC cohorts. In FUSCC cohort 1, our analysis revealed that patients with elevated ^{68}Ga-FAPI-PET SUVmax values exhibited a corresponding increase in SLC38A2 expression (Fig. 4Q). Similarly, in FUSCC cohort 2, tissues from CRLM patient demonstrated significantly higher levels of SLC38A2 expression compared to those without LM (Fig. 4M, N). Furthermore, in FUSCC cohort 3, we observed that CRC tissues with elevated PWAR6 expression were associated with a concomitant upregulation of SLC38A2 (Fig. 4O, P). The TCGA database shows that there is a positive correlation between SLC38A2 and PWAR6 (Supplementary Fig. 3H).

Additionally, we also found that knocking down SLC38A2 significantly reduced the size of subcutaneous tumors and liver metastases in C57BL/6 mice model constructed as previous described (Fig. 4R–U).

Collectively, these findings indicate that myCAF-derived exosome PWAR6 promotes increased glutamine

(See figure on next page.)

Fig. 4 myCAF-derived exo-PWAR6 enhances the glutamine uptake of CRC cells via upregulation of amino acid transporters SLC38A2. **A**, **B** Metabolomics Sequencing of exosomes secreted by myCAFs from CRLM tissues and paired NFs (n = 5 patients). **C**, **D** Evaluation of glutamine uptake, glutamate and α-Ketoglutarate in CRC cells co-cultured with myCAFs after knocking down PWAR6. (n = 5, one of three biological replicates). **E** qRT-PCR to analyze the transcriptional profiling of known glutamine transporters treated with shPWAR6/LvPWAR6 exosomes derived from myCAFs. (n = 3, one of three biological replicates). **F**, **G** Western blot to evaluate the protein level of SLC38A2 in DLD1/HCT116 cells treated with myCAF exosomes. (n = 3, one of three biological replicates). **H** SLC38A2 expression is elevated in metastatic compared to primary tumors, data from GSE41568 (n = 133 patients). **I** Immunofluorescence of NRF2 and SLC38A2. (n = 3, one of three biological replicates). **J**, **L** Evaluation of invasion and stemness of DLD1 Cells after shSLC38A2 treatment using Transwell and spheroid formation assays. Scale bars = 100μm(upper), Scale bars = 50μm(lower). (Representative images are shown, data are from three biologically replicates). **M**, **N** Expression of SLC38A2 in FUSCC Cohort 2 and representative IHC staining images. Scale bars = 50μm. (Representative images are shown, n = 25 patients). **O**, **P** Expression of SLC38A2 in FUSCC Cohort 3 and representative IHC staining images. Scale bars = 50μm. (Representative images are shown, n = 150 patients). **Q** IHC Staining of SLC38A2 in PDOs from patients with varied ^{68}Ga-FAPI-PET SUVmax. Scale bars = 50μm. (Representative images are shown, n = 15 patients). **R**, **S** SLC38A2 knockdown significantly reduces the size of subcutaneous tumors. (n = 5 mice per group). **T**, **U** SLC38A2 knockdown significantly reduces the size of liver metastases. (n = 3 mice per group). Data are shown as mean ± s.e.m. For C-E, J-L, data were analyzed by one-way ANOVA. For H, M-U, data were analyzed by two-tailed Student's t-test. *P* values. $^{*}P < 0.05$, $^{**}P < 0.01$, $^{***}P < 0.001$

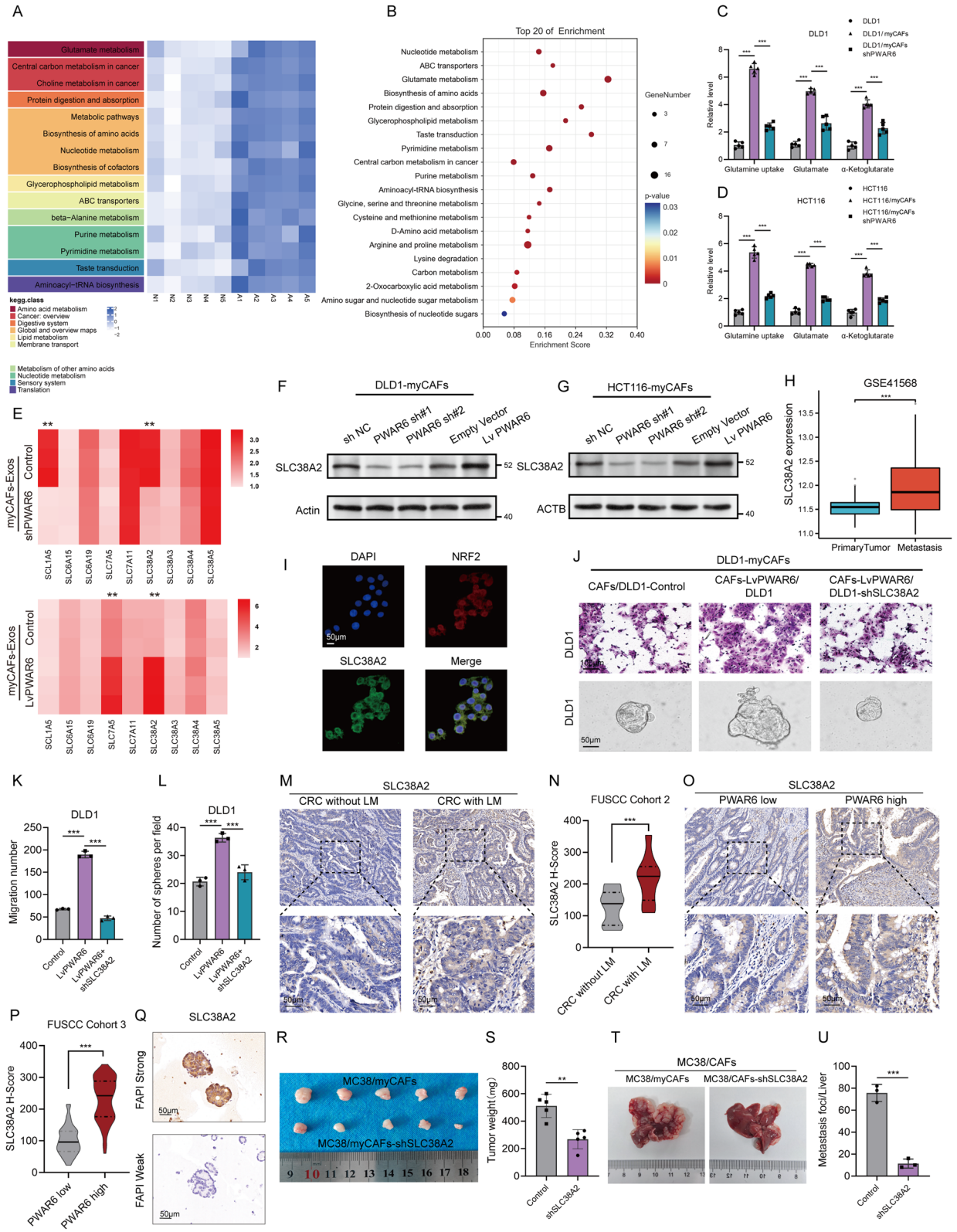

Fig. 4 (See legend on previous page.)

uptake in CRC cells by upregulating the amino acid transporter SLC38A2. Moreover, in vivo and in vitro experiments also demonstrate that myCAF-derived exosome PWAR6-induced upregulation of SLC38A2 can promote the metastasis of CRC cells.

PWAR6 blocks NRF2 ubiquitination and degradation

To elucidate the mechanisms by which myCAF derived PWAR6 modulates glutamine metabolism and enhances CRC metastasis, we firstly cocultured the DLD1 cells with myCAFs (Fig. 5A). Next, biotinylated sense and antisense RNAs corresponding to PWAR6 were synthesized, and subsequent RNA pulldown assays were carried out to elucidate the protein interactome associated with PWAR6 in CRC cells (Fig. 5B). The captured protein complexes were resolved by sodium dodecyl sulfate–polyacrylamide gel electrophoresis (SDS-PAGE) followed by mass spectrometry analysis. After excluding other genes, NRF2 emerged as a plausible candidate protein forming a complex with PWAR6(Fig. 5C). Nuclear fraction assay revealed that NRF2 mainly located in the nuclear (Fig. 5D), FISH assays further substantiated the co-localization of PWAR6 and NRF2 within the cellular context (Fig. 5E). To verify the PWAR6-NRF2 interaction, we performed a pull-down followed by Western blot analysis using an anti-NRF2 antibody, revealing NRF2-PWAR6 complex enrichment in the sense group (Fig. 5F upper part). Additionally, RNA immunoprecipitation (RIP) with an anti-NRF2 antibody and subsequent PCR verified the presence of PWAR6 (Fig. 5F, lower part). Next, we examined the secondary structure of PWAR6 using Vienna RNA (http://rna.tbi.univie.ac.at/) (Fig. 5G). To pinpoint the specific regions of PWAR6 binding to NRF2, we generated a series of truncated PWAR6 variants informed by the secondary structure and employed RNA pulldown combined with Western blot analysis. The results demonstrated that nucleotides 4000–4617 bp of PWAR6 interact with NRF2 (Fig. 5H).

Given the observed interaction between PWAR6 and NRF2 in CRC cells, we sought to explore the regulatory role of PWAR6 on the expression of NRF2. Intriguingly, PWAR6 exhibited no impact on the mRNA abundance of NRF2(supplementary Fig. 5A-B) However, the protein level of NRF2 displayed a significant decrease upon PWAR6 knockdown and a notable increase upon PWAR6 overexpression (Fig. 5I). Next, we treat CRC cells with the protein synthesis inhibitor cycloheximide (CHX, 50ug/mL) for different periods to exam the protein stability of NRF2. Interesting, PWAR6 knockdown decreased the stability of NRF2 and accelerated its degradation (Fig. 5J, K), while PWAR6 overexpression prolonged the half-life of NRF2 degradation (Fig. 5L, M). MG132, a protease inhibitor, can accurately inhibit the ubiquitin-mediated proteasome pathway. Notably, inhibition of the proteasome through MG132 treatment resulted in the accumulation of endogenous NRF2 in CRC cells upon PWAR6 silencing, suggesting that PWAR6 regulated the NRF2 expression at the post-translational level in a ubiquitination-proteasome dependent manner (Fig. 5N).

We next used Western blotting to assess ubiquitination levels, finding that PWAR6 overexpression significantly reduced NRF2 ubiquitination (Fig. 5O). Conversely, PWAR6 knockdown led to a marked increase in NRF2 ubiquitination, with no change in the Input group (Fig. 5P). These results suggest that PWAR6 may inhibit proteasome-dependent degradation of NRF2 in CRC cells. We then analyzed cell migration, stemness, and glutamine uptake in infected cells. NRF2 silencing or overexpression was combined with PWAR6 modulation to explore NRF2's rescue effect on PWAR6-driven functions. Western blotting confirmed NRF2 upregulation

(See figure on next page.)

Fig. 5 PWAR6 blocks NRF2 ubiquitination and degradation. **A** Co-culture of CRC cells and myCAFs before pull-down assay. **B**, **C** Silver stained SDS-PAGE gel of proteins immunoprecipitated by the sense and antisense of PWAR6. The differentially exhibited lanes were used for the mass spectrum. **D** Nucleus-cytoplasm separation experiment showed that NRF2 is mainly located in the nucleus. (n = 3, one of three biological replicates). **E** Representative images of immunofluorescent staining of NRF2 and PWAR6 in DLD1/RKO cells. Scale bars = 50μm. (n = 3, one of three biological replicates). **F** Western blotting assays (upper part) and RIP assay (lower part) of the specific interaction of PWAR6 with NRF2. (n = 3, one of three biological replicates). **G** The secondary structure of PWAR6 is shown as predicated by the centroid method (http://rna.tbi.univie.ac.at/). **H** Truncated PWAR6 fragments interacting with NRF2 in DLD1 cell lysates. (n = 3, one of three biological replicates). **I** Western blot to evaluate the protein level of NRF2 in DLD1/HCT116 cells treated with myCAF exosomes. (n = 3, one of three biological replicates). **J**–**M** Protein stability assay by using cycloheximide (CHX, 50 μg/mL) to treat cells at the different time was performed to evaluate the effect of PWAR6 overexpression (J, K) or knockdown (L, M). (n = 3, one of three biological replicates). **N** Western blot analysis of NRF2 in DLD1/HCT116 cells treated with myCAF overexpression or knockdown exosomes with the proteasome inhibitor MG132 (10 μM). (n = 3, one of three biological replicates). **O**, **P** Co-IP was used to assess NRF2 ubiquitination with and without PWAR6 overexpression (O) or knockdown (P), following MG132 and HA-Ub treatment. (n = 3, one of three biological replicates). **Q**–**T** Transwell assay to evaluate the DLD cell invasion (upper part and R), Scale bars = 100μm, spheroid formation assays to evaluate the DLD cell stemness (middle part and S), PDOs 3D invasion assay to evaluate the invasion of PDOs after knockdown of NRF2 (lower part and T). Scale bars = 50μm. (Representative images are shown, data are from biologically replicates). Data are shown as mean ± s.e.m. For F, K, M and Q-T, data were analyzed by one-way ANOVA. *P* values. **P* < 0.05, ***P* < 0.01, ****P* < 0.001

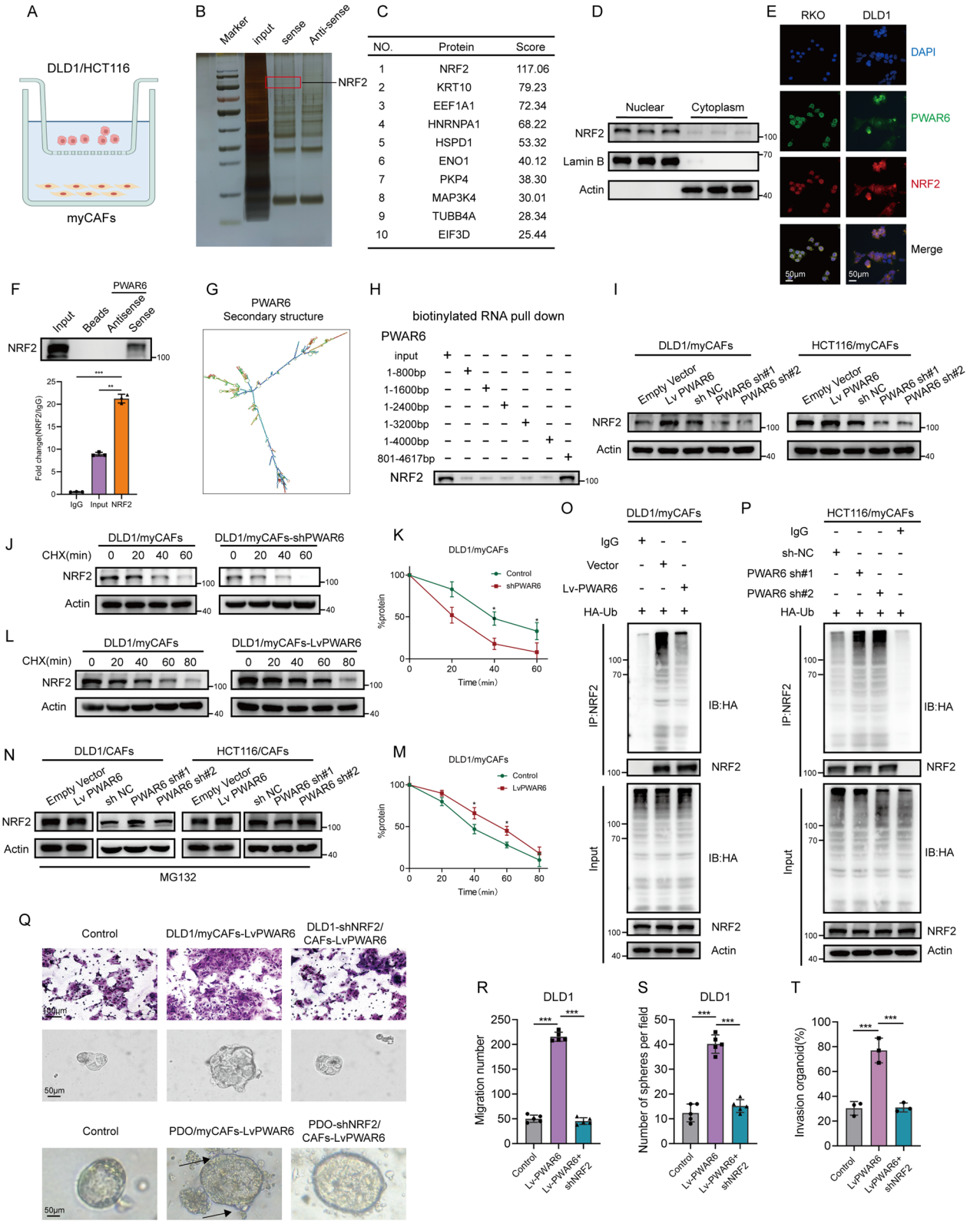

Fig. 5 (See legend on previous page.)

in the Lv-PWAR6 group, reversible by PWAR6 depletion (supplementary Fig. 5C-D). Transwell assays showed that PWAR6 enhanced CRC cell migration, which was blocked by NRF2 depletion (Fig. 5Q upper part, Fig. 5R and supplementary Fig. 5E,F). Sphere-forming assays revealed increased stemness in the Lv-PWAR6 group, reversed by NRF2 silencing (Fig. 5Q middle part, Fig. 5S and supplementary Fig. 5E lower part, supplementary Fig. 5G). Stemness markers such as CD133 and LGR5 followed a similar pattern (supplementary Fig. 5J-K). PDO 3D invasion assays showed that PDOs co-cultured with Lv-PWAR6 CAFs had smooth, protrusive fronts, with robust migration into the 3D matrix, an effect negated by NRF2 depletion (Fig. 5Q lower part and Fig. 5T). Additionally, glutamine uptake was reduced in the sh-PWAR6 group, but NRF2 overexpression rescued this inhibition (supplementary Fig. 5H-I). Overall, these findings demonstrate that PWAR6 promotes cell migration, stemness, and glutamine uptake in CRC cells by upregulating NRF2.

To explore the mechanisms behind PWAR6-driven CRC progression, we examined its interaction with NRF2, a key protein. Using immunoprecipitation (IP) with anti-NRF2 and IgG antibodies, followed by Mass Spectrometry, we identified Keap1 as a significant NRF2-interacting protein (supplementary Fig. 6A), suggesting its role in the ubiquitin–proteasome pathway. Keap1 is known to regulate NRF2 stability by promoting its ubiquitination and degradation via Cul3-based ubiquitin ligase under non-stressed conditions, thus keeping NRF2 levels low and preventing overactivation of downstream genes.

Immunofluorescence further confirmed the co-localization of NRF2 and Keap1 within the cell (supplementary Fig. 6B). We then transfected DLD1 cells with Flag-tagged Keap1 and Myc-tagged NRF2. Co-immunoprecipitation (co-IP) analysis validated the binding between exogenous Keap1 and NRF2, underscoring their strong association (supplementary Fig. 6C-D).

Previous results indicated that PWAR6 inhibits NRF2 ubiquitination, while Keap1 promotes it, suggesting a potential interaction between them. Silencing PWAR6 significantly upregulated Keap1, whereas overexpression of PWAR6 caused a clear downregulation of Keap1 (Fig. 6G, H). These observations suggest a reciprocal regulatory relationship between PWAR6 and Keap1. To further explore Keap1's role in NRF2 downregulation via the ubiquitin–proteasome pathway, we manipulated Keap1 expression and assessed NRF2 ubiquitination levels. Overexpressing Keap1 notably increased NRF2 ubiquitination, while Keap1 knockdown greatly reduced it (supplementary Fig. 6E-F).

To investigate their relationship further, we introduced Flag-tagged Keap1 or Keap1 siRNA into DLD1 cells expressing Lv-PWAR6. Our findings revealed that PWAR6 could partially protect NRF2 from Keap1-mediated ubiquitination and degradation. Quantitative co-immunoprecipitation (co-IP) confirmed that PWAR6 modulates Keap1's impact on NRF2 post-translational ubiquitin modification. Notably, in CRC cells treated with MG132, PWAR6 overexpression reduced the interaction between Keap1 and NRF2, reinforcing PWAR6's regulatory role in this process (supplementary Fig. 6I-J). Besides, knockdown of Keap1 could enhance glutamine uptake of CRC cells (supplementary Fig. 6K-L).

Collectively, we confirmed that Keap1 is a key molecule promoting NRF2 ubiquitination and degradation, while PWAR6 protects NRF2 from Keap1-induced ubiquitination and degradation.

NRF2 promotes glutamine uptake in CRC cells via transcriptionally regulating SLC38A2

Given the co-localization of NRF2 and SLC38A2, we hypothesized that NRF2 might act as a transcription

(See figure on next page.)

Fig. 6 PWAR6 accelerates migration, stemness and glutamine uptake by elevating the expression of NRF2. **A** The average intensity curves for NRF2 signals at TSSs in a region comprising ± 2 Kb in DLD1 and HCT116 cell lines. **B** The IGV shows the CUT&Tag signals of NRF2 at the SLC38A2 promoter. **C** Heatmap of CUT&Tag-seq peaks associated with the NRF2 in DLD1 and HCT116 cell lines, signals are displayed from −2.0 kb to + 2.0 kb surrounding the TSS. Histone H3 as positive control and IgG as negative control. **D** The binding sequence of NRF2 within the promoter region of the SLC38A2 gene. **E** Luciferase assays confirmed that NRF2 regulates SLC38A2 transcription, and PWAR6 overexpression significantly boosts NRF2 activity. (n = 3, one of three biological replicates). **F** Luciferase reporter assays of the transduced DLD1 cells transfected with reporter plasmids containing the SLC38A2 promoter, respectively. Wild type: −2000–0 construct; mutant: −2000–0 constructed with a point mutation at the NRF2 binding site. (n = 3, one of three biological replicates). **G** Westen blot of SLC38A2 after NRF2 knockdown. (n = 3, one of three biological replicates). **H**, **I** Expression of NRF2 in FUSCC Cohort 2 and representative IHC staining images. Scale bars = 50μm. (Representative images are shown, n = 25 patients). **J**, **K** Expression of NRF2 in FUSCC Cohort 3 and representative IHC staining images. Scale bars = 50μm. (Representative images are shown, n = 150 patients). **L** IHC Staining of NRF2 in PDOs from patients with varied 68Ga-FAPI-PET SUVmax. Scale bars = 50μm. (Representative images are shown, n = 15 patients). **M**, **N** NRF2 knockdown significantly reduces the size of subcutaneous tumors. (n = 5 mice per group). **O**, **P** NRF2 knockdown significantly reduces the size of liver metastases. (n = 3 mice per group). Data are shown as mean ± s.e.m. For E, data were analyzed by one-way ANOVA. For F, H-P, data were analyzed by two-tailed Student's t-test. *P* values. $^{*}P < 0.05$, $^{**}P < 0.01$, $^{***}P < 0.001$

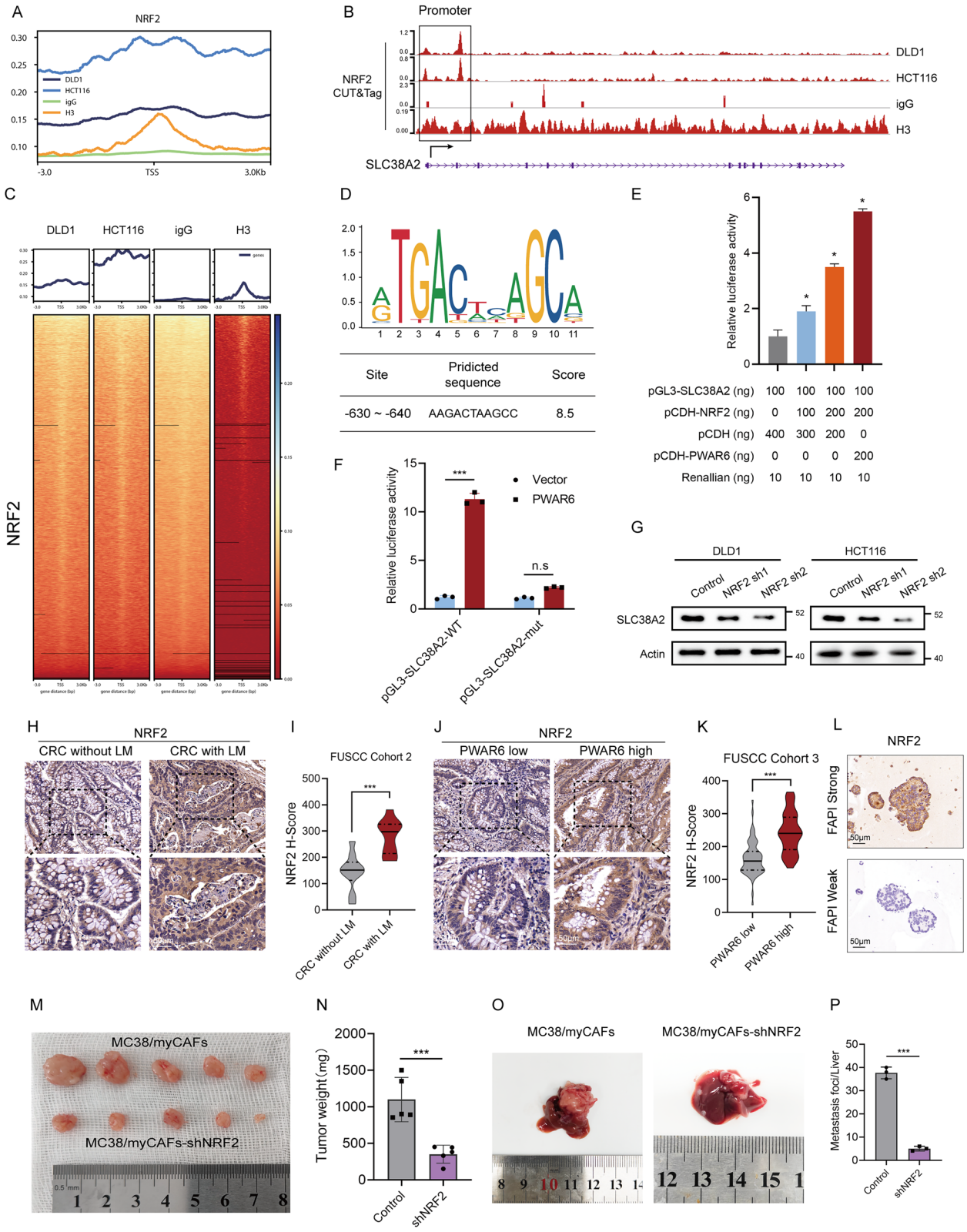

Fig. 6 (See legend on previous page.)

factor by binding to the promoter region of downstream target gene SLC38A2. To test this, we performed a CUT&Tag assay using an anti-NRF2 antibody in DLD1 and HCT116 cells.

Sequences around the CUT&Tag-seq peaks being highly conserved and frequently located in promoter regions. The IGV map clearly indicated that the NRF2 protein occupied the proximal promoter region of SLC38A2 (Fig. 6A, B).The heat map revealed that the peaks were predominantly enriched in TSS regions (Fig. 6C).

According to the CUT&Tag, there is one main binding site in the promoter region of GLUD1 (−1000 to 100 bp), specifically from −630 bp to −640 bp (Fig. 6D). Luciferase reporter assays showed that NRF2 enhances SLC38A2 expression by regulating its transcriptional activity (Fig. 6F). Interestingly, overexpression of PWAR6 further strengthened the transcriptional activity of SLC38A2 (Fig. 6E).

Western blot showed that the knockdown of NRF2 was shown to significantly reduce the levels of SLC38A2 (Fig. 6G).

We then explored the clinical significance of NRF2. In FUSCC cohort 1, we found a positive correlation between high ^{68}Ga-FAPI-PET CT SUVmax values and elevated NRF2 expression, while lower SUVmax values were linked to reduced NRF2 levels (Fig. 6L). In FUSCC cohort 2, CRC patients with LM exhibited significantly higher NRF2 expression compared to those without LM (Fig. 6H, I). In FUSCC cohort 3, we observed a direct association between increased PWAR6 expression and elevated NRF2 levels in CRC tissues, whereas lower PWAR6 expression corresponded with reduced NRF2 levels (Fig. 6J, K).

Subsequently, we co-cultured myCAFs with MC38 cells (Control and shNRF2) and developed subcutaneous and liver metastasis models in C57BL/6 mice using previously described techniques (Fig. 6M–P). Our results demonstrated that NRF2 knockdown in MC38 cells significantly suppressed both subcutaneous tumor growth and liver metastasis.

PWAR6 mediated glutamine deficiency in NK cell promotes tumor immune evasion

In addition to above myCAFs-tumor cells crosstalk, we next asked whether the PWAR6 can metabolically remodel the tumor immune microenvironment (TIME). We further performed cluster analysis focusing on immune cells in the single-cell sequencing database (GSE16655 and GSE178318), it was discerned that the presence of CRLM was associated with a diminished enrichment level of NK cells, CD4+ T cells, CD8+ T cells, B cells and macrophages compared to those CRC patients without LM (Fig. 7A, B).

We next construct subcutaneous tumor and liver metastasis model in C57BL/6 mice as previous described using the PWAR6 overexpression plasmid, followed by flow cytometry assays to examine the impact of PWAR6 overexpression on the TIME. Our findings revealed a significant reduction in NK cell levels, while the changes in CD4+ T cells, CD8+ T cells, and macrophages were less evident (Fig. 7C, D). Immunofluorescence results indicate that PWAR6 overexpression significantly suppresses NK cells in subcutaneous and liver metastatic tumors (Fig. 7E, F). As a result, our subsequent studies will focus on further elucidating the role of NK cells.

To further corroborate our findings, we performed in vitro cellular experiments. Co-culturing NK92MI cells with PWAR6 overexpressing myCAFs did not demonstrate a substantial impact on NK92MI cell activity (Fig. 7G–J). Moreover, the same conclusions were also obtained following co-culture of human NK92MI cells with myCAFs (supplementary Fig. 7A-C). However, when CAFs, CRC cells, and NK92MI cells were co-cultured, the overexpression of PWAR6 significantly attenuated NK cell activity and induced apoptosis (Fig. 7K–N), we

(See figure on next page.)

Fig. 7 SLC38A2 mediated glutamine deficiency in NK cell promotes tumor migration. **A**, **B** Single cell data clustering analysis, data from GSE16655 and GSE178318. (n = 18 patients). **C**, **D** The percentage of immune cells in liver tumors from LvPWAR6 mice. (n = 3 technical replicates, one of three biological replicates). **E** The representative image of NK1.1 staining in subcutaneous tumors. Scale bars = 20μm. (n = 3, one of three biological replicates). **F** The representative image of NK1.1 staining in liver tumors. Scale bars = 20μm. (n = 3, one of three biological replicates). **G** Co-culture of NK91MI cells and myCAFs. (NK92MI in the upper chamber, myCAFs in the lower chamber). **H**, **I** Representative flow cytometry image and statistical graphs of NK92MI apoptosis in the NK92MI/myCAFs co-culture system. (Representative images are shown, data are from three biologically replicates). **J** Representative flow cytometry image of NK92MI proliferation in the NK92MI/myCAFs co-culture system. (n = 3, one of three biological replicates). **K** Co-culture of NK91MI cells, CRC cells and myCAFs. (NK92MI in the upper chamber, CRC cells and myCAFs in the lower chamber). **L**, **M** Representative flow cytometry image and statistical graphs of NK92MI apoptosis in the NK92MI/CRC cell/myCAFs co-culture system. (Representative images are shown, data are from three biologically replicates). **N** Representative flow cytometry image of NK proliferation in the NK92MI/CRC cells/myCAFs co-culture system. (n = 3, one of three biological replicates). **O**, **P** Representative images and statistical graphs for CD107a, Granzyme B, and Perforin detection in NK92MI cells. (Representative images are shown, data are from three biologically replicates). Data are shown as mean ± s.e.m. For C-D, H-J, L-P, data were analyzed by two-tailed Student's t-test. *P* values. **P* < 0.05, ***P* < 0.01, ****P* < 0.001

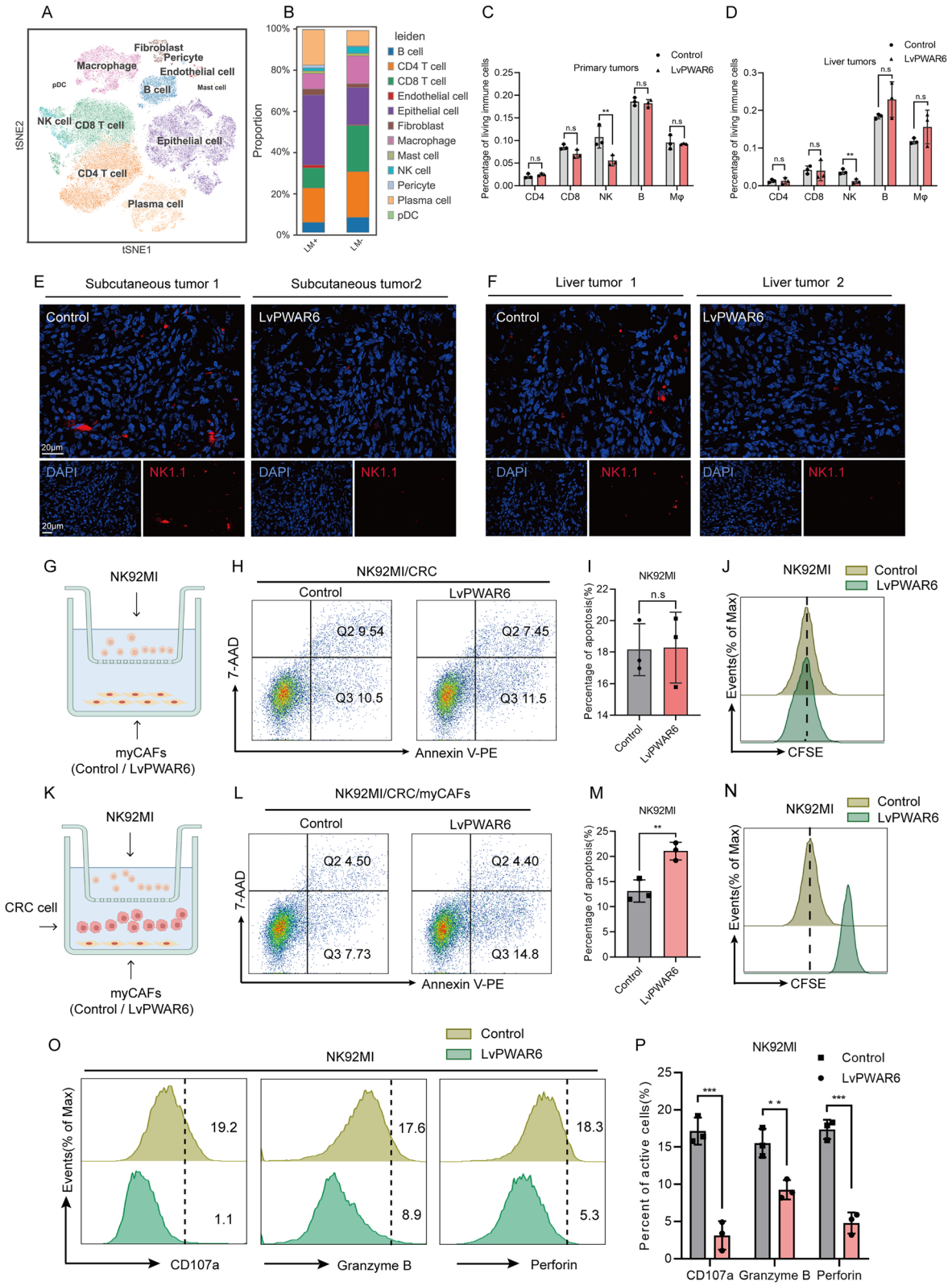

Fig. 7 (See legend on previous page.)

can also observe similar phenomena when using human NK cells (supplementary Fig. 7D-F). These observations indicate that myCAF-derived exosomes PWAR6 exerts a suppressive effect on NK cell function via its interaction with CRC cells.

Previous studies have highlighted the crucial role of glutamine as a key nutrient for supporting NK cell functionality. Building upon our previous results, we postulate that the upregulation of PWAR6 in CRC cells may engender an excessive uptake of glutamine which lead to a diminished pool of available glutamine for utilization by NK cells within the tumor microenvironment, resulting in impaired NK cell activity. Next, we supplemented the co-culture system with exogenous glutamine and re-evaluated NK cell activity. Remarkably, the addition of exogenous glutamine prevented the decline in cell activity, even in the presence of PWAR6 overexpression in myCAFs (supplementary Fig. 7G-H). These results suggest that PWAR6 primarily affects NK cell activity by enhancing the competitive uptake of glutamine between tumor cells and NK cells.

Since PWAR6 predominantly affects the glutamine uptake in CRC cells via SLC38A2, we speculated that CRC cells compete with NK cells for glutamine by overexpressing SLC38A2. We subsequently generated SLC38A2-knockdown CRC cell for co-culture with myCAFs and NK cells. Remarkably, depletion of SLC38A2 restored NK92MI cell activity even when we overexpressed PWAR6 in myCAFs (supplementary Fig. 7I-J). Western blot assay revealed that the level of SLC38A2 in NK92 cells remained essentially unchanged after overexpressing PWAR6(supplementary Fig. 7K). These findings indicate that PWAR6 predominantly influences NK cell activity through SLC38A2-mediated competitive uptake of glutamine by tumor cells and NK cells.

To determine whether the anti-tumor activity of NK92MI cells was also altered in co-cultured with PWAR6 overexpressed myCAFs, we observed minimal impact on the expression of receptors of NK cells as well as NK ligand of CRC cells upon overexpression of PWAR6 (supplementary Fig. 7L-M). Next, we separated NK92MI /human NK cells from co-cultured system and quantified the levels of CD107a, perforin and Granzyme B cells by flow cytometry, these indicators were all significantly downregulated in NK cells co-cultured with PWAR6 overexpressed myCAFs (Fig. 7O, P and supplementary Fig. 7N-O), ELISA experiments revealed a noticeable suppression of the levels of Granzyme B and perforin secreted by NK cells after overexpressing PWAR6(supplementary Fig. 7P-Q), similar conclusion can be drawn by flow cytometry on NK cells extracted from the previous mouse subcutaneous tumor model (supplementary Fig. 7R). We then investigated whether the cytotoxicity of NK cells. NK92MI cells were co-cultured with CRC cells at different ratios, the cytotoxicity of NK92MI cells on CRC cells was significantly inhibited when co-cultured with PWAR6 overexpressed myCAFs, the cytotoxicity of NK92MI cells could be partially restored upon the exogenous addition of glutamine supplementation (supplementary Fig. 7S).

Collectively, our findings demonstrates that PWAR6 induces CRC cells to competitively uptake glutamine from the TME, resulting in glutamine deprivation in NK cells. This glutamine deprivation significantly impairs NK cell activity and cytotoxicity, thereby facilitating tumor progression.

PWAR6 is a potential therapeutic target for CRC

Based on previous critical role of PWAR6 in CRC tumorigenesis, we assessed PWAR6 as a therapeutic target. We targeted PWAR6 with an antisense oligonucleotide (ASO)-based inhibitor, optimized for in vivo application and effective against RNAs. Next, subcutaneous tumor and liver metastasis model in C57BL/6 mice as previous described was firstly constructed using MC38 cells after co-cultured with CAFs, the tumor-bearing mice were randomly divided into three groups: the Control group, the ASO-PWAR6 group, and the ASO-PWAR6 combined with FAPI gavage group (Fig. 8A).

The ASO-PWAR6 inhibitor via tail vein injection significantly diminished subcutaneous tumors and liver metastases tumor burden. Besides, combination of ASO-PWAR6 tail vein injection and FAPI oral gavage demonstrates enhanced the efficacy in alleviating the burden of subcutaneous tumors and liver metastases (Fig. 8B–E).

Histological analyses revealed a progressive increase in NK1.1 expression across the Control group, ASO-PWAR6 group, and ASO-PWAR6 combined with FAPI group in both subcutaneous tumors and liver metastases. Conversely, α-SMA expression demonstrated a corresponding gradual decline across these groups (Fig. 8F, G).

Subsequently, we assessed the levels of CAFs and NK cells in FUSCC Cohort 2. In tissues from CRC patients with high LM/PWAR6 expression, α-SMA expression was markedly elevated, while CD3-/CD56 + expression was relatively diminished. In contrast, CRC patients with low LM/PWAR6 expression exhibited reduced α-SMA levels and more pronounced CD3-/CD56 + expression (Fig. 8H, I).

Discussion

Distant metastasis significantly affects the prognosis of CRC patients. Understanding the mechanisms underlying the metastasis of CRC is crucial for identifying novel drug targets and therapeutic strategies. The stemness of

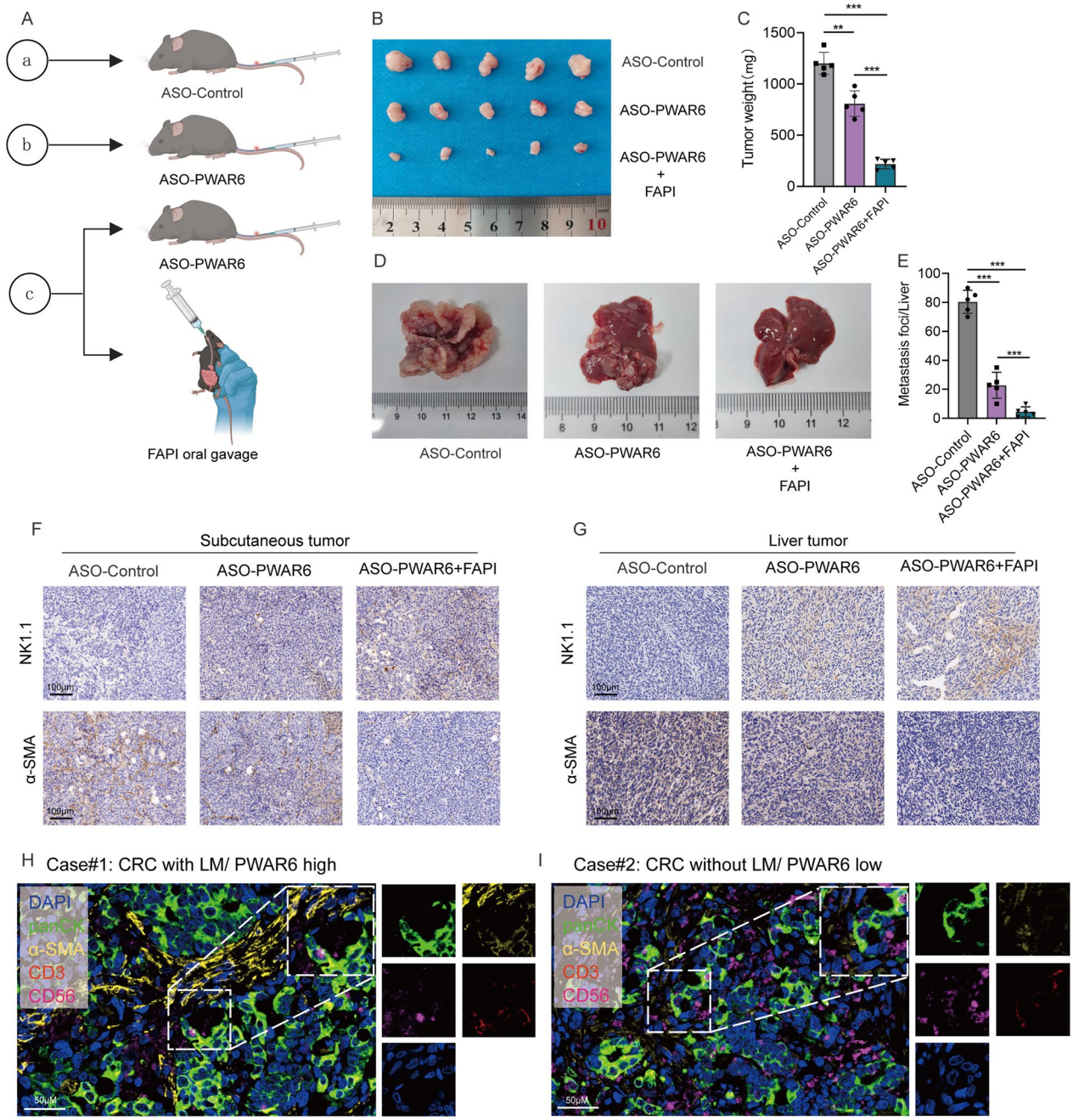

Fig. 8 PWAR6 is a potential therapeutic target for CRC. **A** Graphical diagram of vein tail injection of in vivo optimized PWAR6 inhibitor and FAPI gavage in C57BL/c mice. **B**–**E** Representative images of xenograft tumors (B, C) and liver metastasis (D, E) from each mouse group are shown. Mice with xenograft tumors were treated with either an antisense oligonucleotide control (ASO-Ctrl), an in vivo optimized PWAR6 inhibitor (ASO-PWAR6), or a combination of ASO-PWAR6 and FAPI administered via gavage. (n = 5 mice per group). **F**, **G** Representative images of NK1.1 and α-SMA IHC staining of xenograft tumors and liver metastasis in each group. Scale bars = 100μm. (n = 3, one of three biological replicates). **H**, **I** Representative images of pan-CK, α-SMA, CD3 and CD56 staining in tumor tissues from CRC cancer in FUSCC Cohort2. Scale bars = 50μm. (n = 3, one of three biological replicates). Data are shown as mean ± s.e.m. For B-E, data were analyzed by one-way ANOVA. *P* values. $^{*}P < 0.05$, $^{**}P < 0.01$, $^{***}P < 0.001$

tumor cells are key factors in the initiation and progression of CRC [33]. Our previous work has demonstrated that reducing stemness in PDO models can decrease metastatic potential in CRC. Beyond the characteristics of the tumor cells themselves, there are intricate interactions between tumor cells and various components of

the tumor microenvironment (TME). However, previous research has predominantly focused on intrinsic changes within tumor cells, often neglecting the complex interactions between tumor cells and TME.

myCAFs, among the most prevalent stromal elements in the TME, play a pivotal role in modulating the properties of both tumor cells and TME components. Our findings firstly demonstrated that co-culturing colorectal cancer cells with myCAFs enhances both their metastatic potential and sphere-forming abilities, alongside upregulating stemness-associated markers.

As crucial mediators of substance exchange within the TME, exosomes have been reported to facilitate the transfer of cytokines, miRNAs, and lncRNAs between various cell types. Recent studies have demonstrated that lncRNAs secreted by CAFs play a definitive role in promoting tumor metastasis and enhancing cellular stemness in various cancer type [34, 35]. Here, we successfully isolated myCAFs from CRLM, and found that these myCAFs could transfer the IncRNA through exosomes that promote the migration and metastasis of CRC cells. Among them, PWAR6 was remarkably upregulated in exosomes secreted by myCAFs. In our clinical ^{68}Ga-FAPI-PET/CT imaging and tissue microarray cohorts, we further investigated the relationship between PWAR6 expression and myCAFs, as well as the link between PWAR6 levels and distant metastasis in CRC patients. Interestingly, while our study primarily investigates the role of exosome PWAR6 derived from myCAFs, it raises questions about PWAR6's intracellular distribution and function within myCAFs themselves, particularly regarding its potential influence on exosome packaging and secretion. FISH analysis of CAFs revealed PWAR6 to be predominantly cytoplasmic, suggesting that this localization may facilitate its incorporation into exosomes for release into the tumor microenvironment. However, the exact mechanisms underlying this process warrant further investigation to clarify its regulatory pathways and potential impacts on cancer progression.

Our data compellingly demonstrate that PWAR6 plays a crucial role in facilitating CRC metastasis, confirmed through in vitro and in vivo analyses. Mechanistically, we found that PWAR6 might interact with NRF2 in CRC cells. As a pivotal transcription factor, the abnormal abundance and hyperactivation of NRF2 can promote tumor cell growth and metabolic reprogramming [36, 37]. Based on current research, the protein level of NRF2 is precisely regulated by Keap1 and its associated complex, which mediate the ubiquitination and subsequent degradation of NRF2 [38]. Therefore, our team further investigated the relationship between PWAR6 and the NRF2/Keap1 pathway. The results showed that PWAR6 prevents NRF2 from binding to Keap1 and thereby inhibits its subsequent ubiquitin-mediated degradation. Moreover, our pull-down assays followed by mass spectrometry revealed no direct interaction between PWAR6 and the Keap1 protein. Therefore, we propose that PWAR6 does not directly regulate Keap1 expression. Instead, PWAR6 may promote nuclear translocation and activation of NRF2 by competing with Keap1 for binding, thereby indirectly reducing Keap1 levels. Several studies have also demonstrated that the overactivation of NRF2 could significantly lead to the hypermethylation of the KEAP1 promoter region, further supporting our hypothesis [38].

It has been reported that the aberrant uptake and metabolism of several nutrients are widely observed in cancer cells to meet the demand of rapid proliferation. This metabolic reprogramming is regulated by various molecular mechanisms, including the Keap1/NRF2 pathway [39]. Similarly, different cells within the TME also will compete for essential nutrients like glucose and glutamine, highlighting the dynamic and competitive nature of the TME. However, researches on the processes of substance exchange and nutrient competition among cells within the TME remains insufficient.

Thus, we performed metabolomic sequencing on our paired myCAFs and NFs. The results demonstrated significantly elevated glutamate metabolism in CRLM samples. This phenomenon is highly correlated with the expression levels of PWAR6 and NRF2. To further explore, we found that modulation of PWAR6 transcription markedly affected SLC38A2 expression. SLC38A2 is an important glutamine transporter, and its expression is reported to be elevated in breast and pancreatic cancer [40, 41]. The overexpression of this transporter markedly enhances the uptake and dependency on glutamine and alanine in cancer cells. Meanwhile, increased glutamine utilization in tumor cells may also enhance their stemness [42, 43]. Our study also discovered that by protecting NRF2 from ubiquitin-mediated degradation through PWAR6, NRF2 binds to the promoter region of SLC38A2, thereby activating its transcription, which enhances the tumor cells' ability to scavenge glutamine from the TME and increases their stemness.

As a crucial nutrient within the TME, glutamine is not only essential for the rapid proliferation of tumor cells but also serves as a vital resource for immune cells such as $CD8^+$ T cells, macrophages and NK cells to perform their essential functions [44–46]. In our work, we demonstrated that PWAR6 derived from myCAFs boosts tumor cells' glutamine uptake from the TME, consequently reducing the availability of glutamine for immune cells. Through in vivo and in vitro experiments, we also identified NK cells as the immune cells most affected by PWAR6-mediated glutamine depletion. According to

existing studies, the metabolic imbalance of amino acids such as serine significantly impacts NK cell cytotoxicity [47]. However, the effects of glutamine deprivation on NK cells have not yet been fully elucidated. To further analyze, we employed co-culture systems, flow cytometry, and various analytical techniques to discover that glutamine deprivation in the TME leads to reduced NK cell cytotoxicity, thereby promoting CRC metastasis. This finding not only confirms the crucial role of glutamine in the cytotoxic function of NK cells but also highlights the competitive and dynamic interactions for glutamine among various cells within the TME.

Furthermore, we hypothesize that PWAR6 expression levels are significantly elevated in myCAFs compared to normal fibroblasts, potentially contributing to the pro-metastatic properties of the microenvironment. This differential expression also supports the potential clinical application of ASO-PWAR6, offering a strategy to selectively target and eliminate myCAFs without impairing the function of normal fibroblasts. This specificity could enhance therapeutic efficacy while minimizing off-target effects in normal tissue. This aspect will be further elucidated in our subsequent studies.

In the array of therapeutic strategies targeting RNA in both solid and hematologic tumors, ASOs have shown the most promising clinical potential [48–50]. In our study, we designed ASO sequences targeting PWAR6. Preliminary efficacy assessments were conducted in mouse models, the results indicated that ASOs targeting PWAR6 demonstrated efficacy in inhibiting CRC metastasis and proliferation. However, further experimental validation is required to identify an efficient and precise delivery method and to ensure that the ASO sequence does not affect the expression of normal RNAs.

Conclusion

In summary, we identified a myCAF-specific lncRNA, PWAR6, which enhances stemness, migration and glutamine consumption in CRC cells. Mechanistically, PWAR6 binds to NRF2, preventing its interaction with Keap1 and thereby inhibiting NRF2 ubiquitination and degradation. NRF2, stabilized by PWAR6, functions as a transcription factor to enhance the expression of SLC38A2, thereby facilitating glutamine uptake by CRC cells from the TME. This results in glutamine depletion within the TME and subsequent apoptosis of NK cells.

Supplementary Information

The online version contains supplementary material available at https://doi.org/10.1186/s13045-024-01643-5.

Supplementary Material 1.

Supplementary Material 2.

Acknowledgements
Not applicable.

Author contributions
The studies were designed by GX C, WX D, X W and RJ W. Experiments were performed by HS F, RQ G, J L, YB Z, WQ L, LY H and YC W. Data analysis was carried out by SY T, CY J and HS F. The manuscript was written by HS F, and revised by RQ G and WX D. All authors revised and approved the manuscript.

Funding
This work was supported by the National Natural Science Foundation of China (8217112384) and National Natural Science Foundation of China for Young Scientists (82003317, 82303318).

Availability of data and materials
Data is provided within the manuscript or supplementary information files.

Declarations

Ethics approval and consent to participate
All samples were all collected at Fudan University Shanghai Cancer Center and were approved by the Ethics Committee of Fudan University Shanghai Cancer Center (approval number: 050432-4-1911D). All mouse experiments were approved by the Institutional Animal Care and Use Committee of Fudan university Shanghai Cancer Center (approval number: FUSCC-IACUC-S20210022).

Competing interests
The authors declare no competing interests.

Author details
[1]Department of Colorectal Surgery, Fudan University Shanghai Cancer Center, Shanghai, China. [2]Department of Oncology, Shanghai Medical College, Fudan University, Shanghai, China. [3]Department of Integrative Oncology, Fudan University Shanghai Cancer Center, Shanghai, China. [4]Department of Oncology, Shanghai General Hospital, Shanghai Jiao Tong University School of Medicine, Shanghai, China.

Received: 10 September 2024 Accepted: 21 November 2024
Published online: 18 December 2024

References

1. Siegel RL, Giaquinto AN, Jemal A. Cancer statistics, 2024. CA Cancer J Clin. 2024;74:12–49. https://doi.org/10.3322/caac.21820.
2. Siegel RL, Wagle NS, Cercek A, Smith RA, Jemal A. Colorectal cancer statistics, 2023. CA Cancer J Clin. 2023;73:233–54. https://doi.org/10.3322/caac.21772.
3. Li N, Lu B, Luo C, Cai J, Lu M, Zhang Y, Chen H, Dai M. Incidence, mortality, survival, risk factor and screening of colorectal cancer: a comparison among China, Europe, and northern America. Cancer Lett. 2021;522:255–68. https://doi.org/10.1016/j.canlet.2021.09.034.
4. Ricci-Vitiani L, Lombardi DG, Pilozzi E, Biffoni M, Todaro M, Peschle C, De Maria R. Identification and expansion of human colon-cancer-initiating cells. Nature. 2007;445:111–5. https://doi.org/10.1038/nature05384.
5. Todaro M, Gaggianesi M, Catalano V, Benfante A, Iovino F, Biffoni M, Apuzzo T, Sperduti I, Volpe S, Cocorullo G, et al. CD44v6 is a marker of constitutive and reprogrammed cancer stem cells driving colon cancer metastasis. Cell Stem Cell. 2014;14:342–56. https://doi.org/10.1016/j.stem.2014.01.009.
6. Li H, Dai W, Xia X, Wang R, Zhao J, Han L, Mo S, Xiang W, Du L, Zhu G, et al. Modeling tumor development and metastasis using paired organoids derived from patients with colorectal cancer liver metastases. J Hematol Oncol. 2020;13:119. https://doi.org/10.1186/s13045-020-00957-4.

7. Sedlak JC, Yilmaz ÖH, Roper J. Metabolism and colorectal cancer. Annu Rev Pathol. 2023;18:467–92. https://doi.org/10.1146/annurev-pathmechdis-031521-041113.
8. Cruzat V, Macedo Rogero M, Noel Keane K, Curi R, Newsholme P. Glutamine: metabolism and immune function, supplementation and clinical translation. Nutrients. 2018;10:1. https://doi.org/10.3390/nu10111564.
9. Qiu Y, Cai G, Zhou B, Li D, Zhao A, Xie G, Li H, Cai S, Xie D, Huang C, et al. A distinct metabolic signature of human colorectal cancer with prognostic potential. Clin Cancer Res. 2014;20:2136–46. https://doi.org/10.1158/1078-0432.Ccr-13-1939.
10. Tran TQ, Hanse EA, Habowski AN, Li H, Ishak Gabra MB, Yang Y, Lowman XH, Ooi AM, Liao SY, Edwards RA, et al. α-Ketoglutarate attenuates Wnt signaling and drives differentiation in colorectal cancer. Nat Cancer. 2020;1:345–58. https://doi.org/10.1038/s43018-020-0035-5.
11. Zhang HL, Chen P, Yan HX, Fu GB, Luo FF, Zhang J, Zhao SM, Zhai B, Yu JH, Chen L, et al. Targeting mTORC2/HDAC3 inhibits stemness of liver cancer cells against glutamine starvation. Adv Sci (Weinh). 2022;9: e2103887. https://doi.org/10.1002/advs.202103887.
12. Kalluri R, McAndrews KM. The role of extracellular vesicles in cancer. Cell. 2023;186:1610–26. https://doi.org/10.1016/j.cell.2023.03.010.
13. Kalluri R, LeBleu VS. The biology, function, and biomedical applications of exosomes. Science. 2020. https://doi.org/10.1126/science.aau6977.
14. Hu JL, Wang W, Lan XL, Zeng ZC, Liang YS, Yan YR, Song FY, Wang FF, Zhu XH, Liao WJ, et al. CAFs secreted exosomes promote metastasis and chemotherapy resistance by enhancing cell stemness and epithelial-mesenchymal transition in colorectal cancer. Mol Cancer. 2019;18:91. https://doi.org/10.1186/s12943-019-1019-x.
15. Deng X, Ruan H, Zhang X, Xu X, Zhu Y, Peng H, Zhang X, Kong F, Guan M. Long noncoding RNA CCAL transferred from fibroblasts by exosomes promotes chemoresistance of colorectal cancer cells. Int J Cancer. 2020;146:1700–16. https://doi.org/10.1002/ijc.32608.
16. Ji Q, Zhou L, Sui H, Yang L, Wu X, Song Q, Jia R, Li R, Sun J, Wang Z, et al. Primary tumors release ITGBL1-rich extracellular vesicles to promote distal metastatic tumor growth through fibroblast-niche formation. Nat Commun. 2020;11:1211. https://doi.org/10.1038/s41467-020-14869-x.
17. Yang L, Achreja A, Yeung TL, Mangala LS, Jiang D, Han C, Baddour J, Marini JC, Ni J, Nakahara R, et al. Targeting stromal glutamine synthetase in tumors disrupts tumor microenvironment-regulated cancer cell growth. Cell Metab. 2016;24:685–700. https://doi.org/10.1016/j.cmet.2016.10.011.
18. Zhao H, Yang L, Baddour J, Achreja A, Bernard V, Moss T, Marini JC, Tudawe T, Seviour EG, San Lucas FA, et al. Tumor microenvironment derived exosomes pleiotropically modulate cancer cell metabolism. Elife. 2016;5: e10250. https://doi.org/10.7554/eLife.10250.
19. Yang E, Wang X, Gong Z, Yu M, Wu H, Zhang D. Exosome-mediated metabolic reprogramming: the emerging role in tumor microenvironment remodeling and its influence on cancer progression. Signal Transduct Target Ther. 2020;5:242. https://doi.org/10.1038/s41392-020-00359-5.
20. Maskalenko NA, Zhigarev D, Campbell KS. Harnessing natural killer cells for cancer immunotherapy: dispatching the first responders. Nat Rev Drug Discov. 2022;21:559–77. https://doi.org/10.1038/s41573-022-00413-7.
21. Wu SY, Fu T, Jiang YZ, Shao ZM. Natural killer cells in cancer biology and therapy. Mol Cancer. 2020;19:120. https://doi.org/10.1186/s12943-020-01238-x.
22. Xia L, Oyang L, Lin J, Tan S, Han Y, Wu N, Yi P, Tang L, Pan Q, Rao S, et al. The cancer metabolic reprogramming and immune response. Mol Cancer. 2021;20:28. https://doi.org/10.1186/s12943-021-01316-8.
23. Wang R, Dillon CP, Shi LZ, Milasta S, Carter R, Finkelstein D, McCormick LL, Fitzgerald P, Chi H, Munger J, Green DR. The transcription factor Myc controls metabolic reprogramming upon T lymphocyte activation. Immunity. 2011;35:871–82. https://doi.org/10.1016/j.immuni.2011.09.021.
24. Ma G, Zhang Z, Li P, Zhang Z, Zeng M, Liang Z, Li D, Wang L, Chen Y, Liang Y, Niu H. Reprogramming of glutamine metabolism and its impact on immune response in the tumor microenvironment. Cell Commun Signal. 2022;20:114. https://doi.org/10.1186/s12964-022-00909-0.
25. Herrera M, Berral-González A, López-Cade I, Galindo-Pumariño C, Bueno-Fortes S, Martín-Merino M, Carrato A, Ocaña A, De La Pinta C, López-Alfonso A, et al. Cancer-associated fibroblast-derived gene signatures determine prognosis in colon cancer patients. Mol Cancer. 2021;20:73. https://doi.org/10.1186/s12943-021-01367-x.
26. Nurmik M, Ullmann P, Rodriguez F, Haan S, Letellier E. In search of definitions: cancer-associated fibroblasts and their markers. Int J Cancer. 2020;146:895–905. https://doi.org/10.1002/ijc.32193.
27. Liu T, Han C, Fang P, Ma Z, Wang X, Chen H, Wang S, Meng F, Wang C, Zhang E, et al. Cancer-associated fibroblast-specific lncRNA LINC01614 enhances glutamine uptake in lung adenocarcinoma. J Hematol Oncol. 2022;15:141. https://doi.org/10.1186/s13045-022-01359-4.
28. Zhao L, Chen J, Pang Y, Fu K, Shang Q, Wu H, Sun L, Lin Q, Chen H. Fibroblast activation protein-based theranostics in cancer research: a state-of-the-art review. Theranostics. 2022;12:1557–69. https://doi.org/10.7150/thno.69475.
29. Zhu L, Sun HT, Wang S, Huang SL, Zheng Y, Wang CQ, Hu BY, Qin W, Zou TT, Fu Y, et al. Isolation and characterization of exosomes for cancer research. J Hematol Oncol. 2020;13:152. https://doi.org/10.1186/s13045-020-00987-y.
30. Gao J, Li A, Hu J, Feng L, Liu L, Shen Z. Recent developments in isolating methods for exosomes. Front Bioeng Biotechnol. 2022;10:1100892. https://doi.org/10.3389/fbioe.2022.1100892.
31. Loktev A, Lindner T, Mier W, Debus J, Altmann A, Jäger D, Giesel F, Kratochwil C, Barthe P, Roumestand C, Haberkorn U. A tumor-imaging method targeting cancer-associated fibroblasts. J Nucl Med. 2018;59:1423–9. https://doi.org/10.2967/jnumed.118.210435.
32. Mori Y, Dendl K, Cardinale J, Kratochwil C, Giesel FL, Haberkorn U. FAPI PET: fibroblast activation protein inhibitor use in oncologic and nononcologic disease. Radiology. 2023;306: e220749. https://doi.org/10.1148/radiol.220749.
33. Zhao H, Ming T, Tang S, Ren S, Yang H, Liu M, Tao Q, Xu H. Wnt signaling in colorectal cancer: pathogenic role and therapeutic target. Mol Cancer. 2022;21:144. https://doi.org/10.1186/s12943-022-01616-7.
34. Li Y, Zheng H, Luo Y, Lin Y, An M, Kong Y, Zhao Y, Yin Y, Ai L, Huang J, Chen C. An HGF-dependent positive feedback loop between bladder cancer cells and fibroblasts mediates lymphangiogenesis and lymphatic metastasis. Cancer Commun (Lond). 2023;43:1289–311. https://doi.org/10.1002/cac2.12470.
35. Ren J, Ding L, Zhang D, Shi G, Xu Q, Shen S, Wang Y, Wang T, Hou Y. Carcinoma-associated fibroblasts promote the stemness and chemoresistance of colorectal cancer by transferring exosomal lncRNA H19. Theranostics. 2018;8:3932–48. https://doi.org/10.7150/thno.25541.
36. Rojo de la Vega M, Chapman E, Zhang DD. NRF2 and the hallmarks of cancer. Cancer Cell. 2018;34:21–43. https://doi.org/10.1016/j.ccell.2018.03.022.
37. He F, Ru X, Wen T. NRF2, a Transcription Factor for Stress Response and Beyond. Int J Mol Sci. 2020. https://doi.org/10.3390/ijms21134777.
38. Adinolfi S, Patinen T, Jawahar Deen A, Pitkänen S, Härkönen J, Kansanen E, Küblbeck J, Levonen AL. The KEAP1-NRF2 pathway: Targets for therapy and role in cancer. Redox Biol. 2023;63: 102726. https://doi.org/10.1016/j.redox.2023.102726.
39. Galan-Cobo A, Sitthideatphaiboon P, Qu X, Poteete A, Pisegna MA, Tong P, Chen PH, Boroughs LK, Rodriguez MLM, Zhang W, et al. LKB1 and KEAP1/NRF2 pathways cooperatively promote metabolic reprogramming with enhanced glutamine dependence in KRAS-mutant lung adenocarcinoma. Cancer Res. 2019;79:3251–67. https://doi.org/10.1158/0008-5472.Can-18-3527.
40. Morotti M, Zois CE, El-Ansari R, Craze ML, Rakha EA, Fan SJ, Valli A, Haider S, Goberdhan DCI, Green AR, Harris AL. Increased expression of glutamine transporter SNAT2/SLC38A2 promotes glutamine dependence and oxidative stress resistance, and is associated with worse prognosis in triple-negative breast cancer. Br J Cancer. 2021;124:494–505. https://doi.org/10.1038/s41416-020-01113-y.
41. Parker SJ, Amendola CR, Hollinshead KER, Yu Q, Yamamoto K, Encarnación-Rosado J, Rose RE, LaRue MM, Sohn ASW, Biancur DE, et al. Selective alanine transporter utilization creates a targetable metabolic niche in pancreatic cancer. Cancer Discov. 2020;10:1018–37. https://doi.org/10.1158/2159-8290.Cd-19-0959.
42. Li B, Cao Y, Meng G, Qian L, Xu T, Yan C, Luo O, Wang S, Wei J, Ding Y, Yu D. Targeting glutaminase 1 attenuates stemness properties in hepatocellular carcinoma by increasing reactive oxygen species and suppressing Wnt/beta-catenin pathway. EBioMedicine. 2019;39:239–54. https://doi.org/10.1016/j.ebiom.2018.11.063.
43. Wong CC, Xu J, Bian X, Wu JL, Kang W, Qian Y, Li W, Chen H, Gou H, Liu D, et al. In colorectal cancer cells with mutant KRAS, SLC25A22-mediated

glutaminolysis reduces DNA demethylation to increase WNT signaling, stemness, and drug resistance. Gastroenterology. 2020;159:2163-2180. e2166. https://doi.org/10.1053/j.gastro.2020.08.016.
44. Reinfeld BI, Madden MZ, Wolf MM, Chytil A, Bader JE, Patterson AR, Sugiura A, Cohen AS, Ali A, Do BT, et al. Cell-programmed nutrient partitioning in the tumour microenvironment. Nature. 2021;593:282–8. https://doi.org/10.1038/s41586-021-03442-1.
45. Best SA, Gubser PM, Sethumadhavan S, Kersbergen A, Negrón Abril YL, Goldford J, Sellers K, Abeysekera W, Garnham AL, McDonald JA, et al. Glutaminase inhibition impairs CD8 T cell activation in STK11-/Lkb1-deficient lung cancer. Cell Metab. 2022;34:874-887.e876. https://doi.org/10.1016/j.cmet.2022.04.003.
46. Cluntun AA, Lukey MJ, Cerione RA, Locasale JW. Glutamine metabolism in cancer: understanding the heterogeneity. Trends Cancer. 2017;3:169–80. https://doi.org/10.1016/j.trecan.2017.01.005.
47. Zheng X, Hou Z, Qian Y, Zhang Y, Cui Q, Wang X, Shen Y, Liu Z, Zhou Y, Fu B, et al. Tumors evade immune cytotoxicity by altering the surface topology of NK cells. Nat Immunol. 2023;24:802–13. https://doi.org/10.1038/s41590-023-01462-9.
48. Zhang C, Zhang B. RNA therapeutics: updates and future potential. Sci China Life Sci. 2023;66:12–30. https://doi.org/10.1007/s11427-022-2171-2.
49. Tamm I, Wagner M. Antisense therapy in clinical oncology: preclinical and clinical experiences. Mol Biotechnol. 2006;33:221–38. https://doi.org/10.1385/mb:33:3:221.
50. Ramasamy T, Ruttala HB, Munusamy S, Chakraborty N, Kim JO. Nano drug delivery systems for antisense oligonucleotides (ASO) therapeutics. J Control Release. 2022;352:861–78. https://doi.org/10.1016/j.jconrel.2022.10.050.

Publisher's Note